UNIVERSITY OF CALIFORNIA
RIVERSIDE

Development of ZnO Based Light Emitting Diodes and Laser Diodes

A Dissertation submitted in partial satisfaction
of the requirements for the degree of

Doctor of Philosophy

in

Electrical Engineering

by

Jieying Kong

December 2012

Dissertation Committee:
Dr. Jianlin Liu, Chairperson
Dr. Roger Lake
Dr. Elaine Haberer

The Dissertation of Jieying Kong is approved:

_____

_____

_____

Committee Chairperson

University of California, Riverside

ACKNOWLEDGEMENTS

I would like to thank my advisor Prof. Jianlin Liu for the guidance and support from during the course of my Ph.D. study and research. He is an extremely helpful and encouraging advisor, who helped me through difficult times in my research work. I would also like to thank my committee members, Dr. Lake, and Dr. Haberer for their dedication on reviewing my work.

Of all the wonderful people that I have met throughout my graduate studies I would really like to acknowledge my lab mates and colleagues that helped me the most. I would like to thank Mario Olmedo, Sheng Chu, Jian Huang, Zheng Zuo, Lin Li, Jingjian Ren, Monzur Morshed, Zheng Yang, Bei Li, Ning Zhan, Huimei Zhou, Jing Qi, and. Without the pleasant working environment you guys created I would not have had such a great time.

Finally I would like to thank my parents, and the rest of my family for their support and understanding that a doctorate takes time and sacrifice. Their support was invaluable and this would not have happened without them.

ABSTRACT OF THE DISSERTATION

Development of ZnO Based Light Emitting Diodes and Laser Diodes

by

Jieying Kong

Doctor of Philosophy, Graduate Program in Electrical Engineering
University of California, Riverside, December 2012
Dr. Jianlin Liu, Chairperson

ZnO based homojunction light emitting diode, double heterojunction light emitting diode, embedded heterojunction random laser diode and Fabry-Perot nanowire laser devices were fabricated and characterized. A variety of measurements such as X-ray diffraction, photoluminescence, scanning electron microscope and secondary ion mass spectrometry were used to characterize material properties. Current-voltage, capacitance-voltage and electroluminescence measurements were used to characterize device performance.

ZnO p-n junction diode was successfully grown on Si substrate by using Sb and Ga for p-type and n-type dopants respectively. The diode device was fabricated by using standard photolithography process. Due to the improved material quality, dominant

ultraviolet light emission from ZnO homojunction diode was firstly observed and the emission properties were studied with increased injection currents. To improve the efficiency, A MgZnO/ZnO double heterojunction structure was realized by molecular beam epitaxy growth on Si substrate. Compared to homojunction structure, the carrier confinement effect in double heterojunction structure gave rise to larger output power at same injection current. With smaller heterojunction well size, ZnO based random laser diode was developed. A thin MgZnO/ZnO/MgZnO well embedded in a ZnO p-n junction was realized by molecular beam epitaxy growth. Random lasing emissions were observed at different injection currents at room temperature. Lasing mechanism was discussed and proved by deep investigation of its nano-structure. Fabry-perot type laser was also developed in our lab, to lower lasing threshold, distributed Bragg reflector was proposed. Vertically aligned ZnO nanowires were firstly successfully grown on distributed Bragg reflectors made of SiO_2/SiN_x alternative layers. By means of optical excitation, Fabry-Perot type lasing was observed and characterized. Compared to the same length nanowires without distributed Bragg reflectors, better lasing performance was achieved. The discussion of lasing mechanism revealed the function of distributed Bragg reflectors in improving lasing performance.

Table of Contents

List of figures

Chapter I: Introduction

1.1 Introduction to Light emitting diode and laser diode

The light emitting diode (LED) was discovered in 1904, when the silicon carbide was used to fabricate contact rectifier devices. [1] Although the level of light emission from such devices is very small, it paves way for future LED development. The past few decades have brought a continuing and rapidly evolving sequence of technological revolutions, particularly in the digital area, which has dramatically changed many aspects of our daily lives. The LED and laser diode (LD) are considered the ultimate general source of continuous light due to its high luminescence efficiency, quick response time, and long lifetime. Reduction of maintenance will be achieved, for example, by using colored LED as traffic signals instead of traditional lamp.

The key mechanism of LED is band-to-band recombination (radiation). For this reason, direct band gap materials are normally used to fabricate LED and LD devices. Table 1.1 listed commercially or commonly used materials for different wavelengths LEDs. Ultraviolet (UV) light emitters are essentially important for realizing white color LED, which illuminates from UV excited phosphors. Other than solid-state lighting, UV light emitters are in strong demand in areas of information and biotechnologies for a variety of applications, such as, information storage, secure communications, and biosensors. [2-5] UV business brings a big market with traditional UV lamp technology. Thanks to its compactness, lower cost of ownership and environmental friendly composition, it is expected that UV LED and LD will replace traditional lamps and also will open the door to many new applications, such as DVD storage.

	Color	Wavelength[nm]	Semiconductor material
	Infrared	$\lambda > 760$	GaAs, AlGaAs
	Red	$610 < \lambda < 760$	AlGaAs, GaAsP,AlGaInP
	Orange	$590 < \lambda < 610$	GaAsP, AlGaInP, GaP
	Yellow	$570 < \lambda < 590$	GaAsP, AlGaInP, GaP
	Green	$500 < \lambda < 570$	InGaN/GaN, GaP, AlGaInP, AlGaP
	Blue	$450 < \lambda < 500$	ZnSe, InGaN
	Violet	$400 < \lambda < 450$	InGaN
	Purple	multiple types	Dual blue/red LEDs, blue with red phosphor, or white with purple plastic
	Ultraviolet	$\lambda < 400$	Diamond, Boron nitride AlN, AlGaN, AlGaInN

Table 1.1 Semiconductor materials for different wavelengths LEDs

1.2 Introduction to ZnO based LED and LD

Among the available wide bandgap materials such as diamond and GaN, ZnO is an interesting and potential candidate for the use as an UV light emitter. Diamond is an indirect bandgap material, which results in low emission efficiency.[6] GaN is a direct bandgap material with a bandgap energy of 3.39 eV, but the exciton have binding energy of 25 meV, which is comparable to thermal noise at room temperature.[7-9] ZnO has both advantages, it has direct bandgap of 3.37 eV and a large exciton binding energy of 60 meV, making it to be the best candidate in the area of UV LED and LD. [10-13] The availability of large-area ZnO substrates and the possibility of wet etching also favor the fabrication of ZnO-based optical devices.[14,15]

Although the history of ZnO research goes back to 1930s, [16-23] p-type doping of ZnO becomes the main hindrance in the development of ZnO based optoelectronic devices.[24] Intrinsic defects such as Zn interstitials, oxygen vacancies and H incorporation evolve in the ZnO material during growth. These defects form shallow and deep donor levels due to which, intrinsic ZnO shows very strong n-type conductivity, making p-type material a challenge. Therefore, previous efforts on ZnO p-n junctions are mostly made from n-type ZnO and other p-type semiconductors such as SiC, GaN, $SrCu_2O_2$ and so on. [25-27] The benefit of making those heterojunction LEDs is that it is easy to obtain a device, however, the chemical and crystallographic differences between ZnO and other materials give rise to the formation of interfacial defects, leaving negative impact on optical and electrical properties of diodes. Several groups have also reported p-n homojunction ZnO LEDs by various doping element such as N,[28-30] P,[31-33]

As,[34,35] and other specific techniques, which showed rectifying I-V characteristics and electroluminescence (EL) at room temperature. Our group have successfully developed a process to produce reliable p-type ZnO layers with good optical properties by Sb doping and adopting a post-deposition thermal annealing process to activate the dopants in the ZnO films. [36,37] After that, we also successfully developed good Ohmic contacts to n- and p-type ZnO films, which showed linear current-voltage (I-V) characteristics with low specific contact resistances. [38,39] All the achievements paved way of developing high efficiency LED and LD devices. Here we focus on designing and optimizing device structures for higher output efficiency.

1.3 Organization of dissertation

This dissertation is organized as follows. Chapter I introduces a brief history of research on the ZnO semiconductor and the goal of this research. A review of the fundamental properties of ZnO semiconductor material, growth techniques and characterization methods is presented in Chapter II. Then, Chapter III describes the development of Sb-doped p-type ZnO/Ga-doped n-type ZnO homojunction LEDs. Chapter IV presents the high efficiency design of heterojunction LED. Chapter V focuses on the design of lower threshold Fabry-Perot laser by using distributed Bragg reflectors (DBR). Chapter VI describes the development of ZnO random laser diodes and DBR assisted nanowire laser diodes. Chapter VII is conclusion of all the work.

1.4 Reference

[1] H. J. Round, Electrical World, 49, 309 (1907)

[2] R. F. Service, Science 276, 895 (1997).

[3] S. Nakamura, T. Mukai, and M. Senoh, Appl. Phys. Lett. 64, 1687 (1994).

[4] G. Rostky, Electronic Engineering Times, 944, 10 (1997)

[5] R. L. Shepherd, W. S. Yerazunis, L. T. King and D. Diamond, Sensors Journal, IEEE, 6, 861 (2006)

[6] S. Nakamura, Science 281, 956 (1998).

[7] J. Han, M. H. Crawford, R. J. Shul, J. J. Figiel, M. Banas, L. Zhang, Y. K. Song, H. Zhou, and A. V. Nurmikko, Appl. Phys. Lett. 73, 1688 (1998).

[8] H. Amano, T. Asahi and I. Akasaki, Jpn. J. Appl. Phys. 29, L205 (1990)

[9] I. Akasaki, H. Amano, S. Sota, H. Sakai, T. Tanaka and M. Koike, Jpn. J. Appl. Phys. 34, L1517 (1995)

[10] K. Watanabe, T. Taniguchi, and H. Kanda, Nature Mater. 3, 404 (2004).

[11] H. Kawazoe, M. Yasukawa, H. Hyodo, M. Kurita, H. Yanagi, and H. Hosono, Nature 389, 939 (1997).

[12] U. Ozgur, Ya. I. Alivov, C. Liu, A. Teke, M. A. Reshchikov, S. Dogan, V. Avrutin, S. J. Cho, and H. Morkoc, J. Appl Phys 98, 041301 (2005).

[13] C. Klingshirn, phys. stat. sol. (b) 244, No. 9, 3027– 3073 (2007).

[14] S. Koizumi, K. Watanabe, M. Hasegawa, and H. Kanda, Science 292, 1899 (2001).

[15] S. Nakamura, Science 281, 956(1998).

[16] H. J. Yearian, Phys. Rev. 48 (7): 631-639 (1935).

[17] H. M. James, V. A. Johnson, Electron distribution in ZnO crystals, Phys. Rev. 56 (1): 119-119 (1939).

[18] C. Klingshirn, Phys. Stat. Sol. (b) 244, No. 9, 3027– 3073 (2007).

[19] C. W. Bunn, Proc. Phys. Soc. London 47, 835 (1935).

[20] T. J. Gray, J. Am. Ceram. Soc. 37, 534 (1954).

[21] H. E. Brown, Zinc Oxide Rediscovered, The New Jersey Zinc Company, New York (1957) and Zinc Oxide, Properties and Applications (1976).

[22] G. P. Mohatny and L. V. Azaroff, J. Chem. Phys. 35, 1268 (1961).

[23] H. Heiland, E. Mollwo, and F. Stöckmann, Solid State Phys. 8, 191 (1959).

[24] D. C. Look, Mater. Sci. and Eng. B 80, 383 (2001).

[25] H. Ohta, M. Orita, M. Hirano, H. Hosono, Appl. Phys. Lett. 77,475 (2000),

[26] Y. I. Alivov, J. E. V. Nostrand, D. C. Look, M. V. Chukichev, B. M. Ataev, Appl. Phys. Lett. 83, 2943 (2003).

[27] Ya. I. Alivov, U. Ozgur, S. Dogan, D. Johnstone, V. Avrutin, N. Onojima, C. Liu, J. Xie, Q. Fan, and H. Morkoç, Appl. Phys. Lett. 86, 241108 (2005)

[28] A. Tsukazaki, A. Ohtomo, T. Onuma, M. Ohtani, T. Makino, M. Sumiya, K. Ohtani, S. F. Chichibu, S. Fuke, Y. Segawa, H. Ohno, H. Koinuma, and M. Kawasaki, Nat. Mater. 4, 42 (2005).

[29] D. C. Look, D. C. Reynolds, C. W. Litton, R. L. Jones, D. B. Eason, and G. Cantwell, Appl. Phys. Lett. 81, 1830 (2002).

[30] K. W. Liu, D. Z. Shen, C. X. Shan, J. Y. Zhang, B. Yao, D. X. Zhao, Y. M. Lu, and X. W. Fan, Appl. Phys. Lett. 91, 201106 (2007).

[31] F. X. Xiu, Z. Yang, L. J. Mandalapu, J. L. Liu, and W. P. Beyermann, Appl. Phys. Lett. 88, 052106 (2006).

[32] J. H. Lim, C. K. Kang, K. K. Kim, I. K. Park, D. K. Hwang, and S. J. Park, Adv. Mater. 18, 2720 (2006).

[33] D. K. Hwang, M. S. Oh, J. H. Lim, C. G. Kang, and S. J. Park, Appl. Phys. Lett. 90, 021106 (2007).

[34] Y. R. Ryu, T. S. Lee, J. A. Lubguban, H. W. White, B. J. Kim, Y. S. Park, and C. J. Youn, Appl. Phys. Lett. 88, 241108 (2006).

[35] J. C. Sun, J. Z. Zhao, H. W. Liang, J. M. Bian, L. Z. Hu, H. Q. Zhang, X. P. Liang, W. F. Liu, G. T. Du, Appl. Phys. Lett. 90, 121128 (2007)

[36] F. X. Xiu, Z. Yang, L. J. Mandalapu, D. T. Zhao, J. L. Liu, and W. P. Beyermann, Appl. Phys. Lett. 87, 152101 (2005)

[37] L. J. Mandalapu, F. X. Xiu, Z. Yang, and J. L. Liu, Appl. Phys. Lett. 88, 112108 (2006).

[38] L. J. Mandalapu, Z. Yang, F. X. Xiu, and J. L. Liu, Appl. Phys. Lett. 88, 092103 (2006).

[39] L. J. Mandalapu, F. X. Xiu, Z. Yang, and J. L. Liu, J. Appl. Phys. 102, 023106 (2006)

Chapter II Overview of ZnO growth and characterization techniques

2. 1. Properties of zinc oxide semiconductor

ZnO has many attractive characteristics for electronic and optoelectronic devices. The comparison with its main competitor GaN is listed in Table 2.1[1-7] The direct bandgap energy of 3.37 eV is similar to that of GaN, which makes it operate in the UV to blue wavelengths. The exciton binding energy of 60 meV for ZnO, is much larger than 25 meV for GaN; making ZnO more potential in enhancing the efficiency and realization of room temperature LDs. The room-temperature electron Hall mobility in single-crystal ZnO is ~200 cm^2V^{-1}, slightly lower than that of GaN. ZnO exhibits better radiation resistance than GaN for possible devices used in space and nuclear applications. [8] ZnO can be grown on inexpensive substrates, such as glass and Si at relatively low temperatures, and it is easy to achieve nanowire structures. [9-15] These structures are ideal for detector applications due to its large surface area-to-volume ratio. Bandgap engineering for ZnO to get different direct band gap by alloying with materials such as MgO and CdO is still under research, while for GaN, Al, Ga, In alloying technique is more mature.

Property	GaN	ZnO
Direct bandgap energy (eV)	3.4	3.4
Electron mobility ($cm^2/V{\cdot}s$)	220	205
Hole mobility ($cm^2/V{\cdot}s$)	10	5.50
Electron effective mass	0.27 m_0	0.24 m_0
Hole effective mass	0.80 m_0	0.59 m_0
Exciton binding energy (meV)	25	60

Table 2.1. Basic parameters of ZnO and GaN

The most common ZnO crystal is in the wurtzite structure, as shown in Fig. 2.1. This is a hexagonal lattice, unit cell are a=3.2495 Å and c=5.2069 Å; these depend slightly on stoichiometry deviation. The density is 5.605 g/cm3, corresponding to 4.21×10^{22} molecules per cm^3. [16] The lattice structure is belonging to the space group P63mc, and is characterized by two interconnecting sublattices of Zn^{2+} and O^{2-}, such that each Zn ion is surrounded by a tetrahedra of O ions, and vice-versa. The Zn-O bond also possesses very strong ionic characteristic, and thus ZnO lies on the borderline between being classified as a covalent and ionic compound, with an ionicity of *fi* =0.616 on the Phillips ionicity scale. [17]

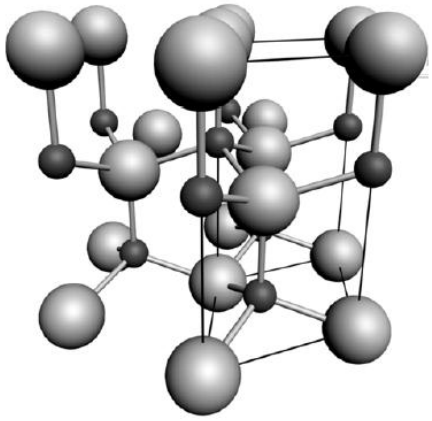

Figure 2.1 The hexagonal wurtzite structure of ZnO. O atoms are shown as large white spheres, Zn atoms as smaller black spheres. One unit cell is outlined for clarity.

Additional to the wurtzite phase, ZnO is also known to crystallize in the hexagonal zincblende and cubic rocksalt (NaCl) structures. Zincblende ZnO is stable only by growth on cubic structures, [18-21] which are unstable and have no application on LED and LD devices. [22]

Bandgap engineering is important for device development. By alloying semiconductor with another material of different bandgap, the bandgap of the resultant alloy material can be finely tuned, thus affecting the wavelength of light emissions. For GaN, AlN and InN are typical alloys to make successful quantum well structures. It was one of the most important steps for achieving commercial blue LEDs. In the case of ZnO, alloying with MgO and CdO is an effective means of increasing or decreasing the energy bandgap, respectively. [23-32] For obtaining n-type and p-type ZnO thin films, dopants like Ga, Al, N, B, In, Si, Ge are used. [33-43] Ga element was used in our growth as an n-type donor since it is less susceptible to oxidize and makes deformation of the ZnO lattice

small even at high Ga concentrations. [33] For p-type doping, there is still no widely used dopants, we used Sb dopant and achieved p-type ZnO.

2.2 Optical Properties of Undoped ZnO

ZnO is a direct bandgap semiconductor since the topmost of valence and the lowest of conduction bands are at the same point in the Brillouin zone, namely at k = 0, i.e. at the Γ-point as shown in the Fig.2.2. The lowest conduction band is formed from the empty 4s states of Zn^{2+} or the anti-binding sp3 hybrid states. The valence band originates from the occupied 2p orbitals of O^{2-} or the binding sp3 orbitals and is split without spin under the influence of the hexagonal crystal field into two states. Inclusion of spin gives a further splitting due to spin-orbit coupling into three two-fold-degenerate sub-valence band of symmetries as shown in Fig. 2.2. The valence bands are labeled from higher to lower energies as A, B, and C bands. However, controversies exist over the ordering of the valence band. [44-46]

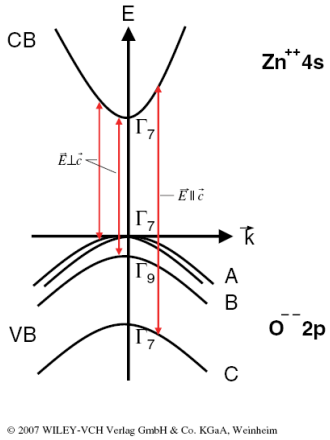

Figure 2.2 Valence and conduction bands of ZnO in the vicinity of the fundamental band gap.

Optical properties of semiconductor material are important for making optoelectronic devices. The optical properties of a semiconductor can be classified into intrinsic and extrinsic properties. Intrinsic refers to optical transitions between valence and conduction bands while extrinsic optical transitions are related to levels created by defects or dopants. The important optical transitions are band to band transitions. When an electron is excited from valence band to conduction band, a hole is left behind in the valence band and coulomb attraction exists between the electron and its corresponding hole. The exciton results from the binding of the electron with its hole; as a result, the exciton has slightly less energy than the unbound electron and hole and it follows a hydrogenic wavefunction. Excitons are classified into free and bound excitons. In high-quality samples with low impurity concentrations, the free exciton can also exhibit excited states, in addition to their ground-state transitions. The near-band-gap intrinsic absorption and emission spectrum is dominated by transitions from three valence bands. The related free exciton transitions from the conduction band to these three valence bands denoted by *A* (heavy hole), *B* (light hole), and *C* (crystal-field split band) or vice versa can occur. Bound excitons manifest as extrinsic optical transitions, which are usually related to dopants or defects, and create discrete electronic states in the band gap. The introduced states in the material therefore influence both optical absorption and emission processes. In theory, excitons could be bound to neutral or charged donors and acceptors. These two classes of bound excitons are the most important cases for direct band-gap materials. In high-quality bulk ZnO substrates, the neutral shallow donor bound exciton usually dominates because of the presence of donor levels introduced due to unintentional

(or doped) impurities and shallow donor like defects. In samples containing acceptors, the acceptor bound exciton is typically observed. The recombination of bound excitons typically gives rise to sharp lines with a photon energy characteristic to each defect. Many sharp donor and acceptor bound exciton lines have been reported in a narrow energy range from 3.348 to 3.374 eV in ZnO. When both donor and acceptor states are present, a donor-acceptor pair (DAP) transition occurs and is one of the important characteristics of p-type film.[47] All these optical transitions also have temperature dependence characteristic showing either a red or blue shift with varying temperature.

2. 3 ZnO growth method

ZnO thin films and nanowires are grown by various techniques, including sputtering deposition, molecular beam epitaxy (MBE), [48-50] chemical vapor deposition (CVD), [51-53] pulsed laser ablation (PLD), [54-57] atomic layer deposition, [58,59] reactive sputtering and spray pyrolysis. [60-62] Both n-type and p-type materials have been reported. ZnO thin films can be grown on a wide range of substrates such as sapphire, Si, GaN, and even inexpensive glass. ZnO can be grown at relatively low temperatures as compared to other wide bandgap semiconductors. Inexpensive substrate and low-temperature growth make product manufacturing cost less.

2.3.1 MBE

The ZnO films were grown by solid source MBE systems. The sources included effusion cells of Zn and various dopants such as Ga, Sb, Mg etc. Oxygen plasma was generated by radio-frequency activation in the SVTA MBE system. The MBE system has two main chamber regions namely, the load lock and growth chamber. The substrates

after cleaning are loaded into load lock, which are then transferred into the high vacuum growth chamber on to a manipulator, which helps in loading the sample in and out, rotates the sample during growth and measures the growth temperature using the thermocouple attached to it. The growth chamber is typically maintained at the pressure range of 10^{-8}–10^{-11} torr. The substrates used for ZnO growth in this dissertation is Si or sapphire wafer. Using sapphire substrates gives the advantage of eliminating any substrate contribution on the device performance, while using the Si substrate gives the possibility of integrating the ZnO devices with the existing advanced Si technology. Si is also much cheaper than sapphire substrates. Generally we use the maximum oxygen flow rate of 5 sccm (cubic centimeter per minute), corresponding to a chamber pressure of 1.7×10^{-4} Torr. The typical growth procedure is described as follows:

1. Substrate cleaning

   Silicon substrate: Dip into H_2SO_4: H_2O_2=3:1 for 1 min, then dip in 5% HF acid for 1 min. Repeat this for 3 times, and then washed by DI water and dried with nitrogen gas.

   Sapphire substrate: aqua regia solution HCl: HNO3=3:1 at 100 °C for 30 min to remove surface contaminants and scratches, and then they were dried with nitrogen gas.

2. Thermal cleaning

   Substrates were then transferred in to growth chamber, heated to 800℃ for 20 min to further remove the particle contaminations on the substrates.

3. Sample growth

Start to grow ZnO samples at appropriate temperatures of 400℃ to 700℃. The growth rate is generally 100 nm to 200 nm /hour.

4. Post annealing to activate the dopant.

2.3.2 CVD

CVD is used to produce high-purity, large scale ZnO nanowires. It is a home-made atmospheric pressure CVD, which consists of a temperature controller, a furnace, incoming gas controller and exhaust gas controller, as shown in Fig. 2.3.

In ZnO CVD process, the wafer is exposed 2 cm away to Zn powder, which react with the incoming O_2 on the substrate surface to produce the desired deposit. Active reaction gas is a mixture of O_2 and Ar (0.5%:99.5% in volume), carrier gas is N_2. Volatile by-products are removed by gas flow through the reaction chamber.

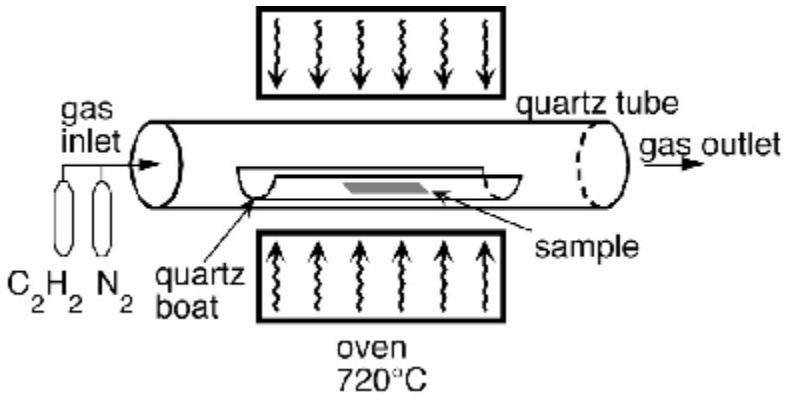

Figure 2.3 CVD furnace setup

2.3.3 ALD deposition

Atomic layer deposition (ALD) is a self-limiting, sequential surface chemistry technique that deposits conformal thin-films of materials onto substrates of varying compositions. ALD is similar in chemistry to chemical vapor deposition (CVD), except

that the ALD reaction breaks the CVD reaction into two half-reactions, keeping the precursor materials separate during the reaction. Due to the characteristics of self-limiting and surface reactions, ALD film growth makes atomic scale deposition control possible. By keeping the precursors separate throughout the coating process, atomic layer control of film growth can be obtained as fine as ~0.1 Å (10 pm) per cycle. Separation of the precursors is accomplished by pulsing a purge gas after each precursor pulse to remove excess precursor from the process. A typical deposition cycle of Al_2O_3 is using both water and $AlCl_4$ as the precursors. First water is pulsed from the source to the growth chamber, then a set time is waited until the substrate surface is fully covered. After that time has passed, the remaining water is pumped out and the $AlCl_4$ sourced is pulsed in. The second precursor reacts with the water to create HCl. After the next water pulse the first layer of Al_2O_3 is formed.

2.4 Device fabrication

Standard LED device fabrication includes photolithography, etching, metal deposition and annealing steps. Kark Suss mask aligner with ultraviolet light source was used for exposure while AZ400K developed the exposed photoresist. Most acid or base could be used for defining mesa. Phosphoric-acetic, hydrochloric acid and ammonium chloride hydroxide buffer base were used. Typical device sizes for fabricating p-n junction diodes were 250 μm x 250 μm or 500 μm x 500 μm or 800 μm x 800 μm while transmission line patterns, used for obtaining specific contact resistivity were 50 μm x 75 μm in size with different spacing. Metal evaporation was carried out using an e-beam evaporator and the samples were given a rapid thermal annealing treatment in N_2

environment (to protect from contamination) if Ohmic contacts were to be formed or the contact resistivity was to be lowered.

2.4.1 Photolithography

Photolithography is the process of transferring geometric shapes on a mask to the surface of a silicon wafer. The steps involved in the photolithographic process are wafer cleaning, barrier layer formation, photoresist application, soft baking, mask alignment, exposure, development, and hard-baking. In the first step, the wafers are chemically cleaned to remove particulate matter on the surface as well as any traces of organic, ionic, and metallic impurities. After that, photoresist is applied to the surface of the wafer. Positive photoresist, AZ5214 is spin-coated for defining mesa and for making contacts by acetone lift-off. The spin speed is controlled to be at 4000 ramp/min, at which speed the thickness of photoresisit is within the range of 1.3 to 1.5 um. For positive resists, the resist is exposed with UV light wherever the underlying material is to be removed. In these resists, exposure to the UV light changes the chemical structure of the resist so that it becomes more soluble in the developer. The exposed resist is then washed away by the developer solution AZ 400K, leaving windows of the bare underlying material. The mask, therefore, contains an exact copy of the pattern which is to remain on the wafer.

2.4.2 E-beam evaporation

In evaporation the substrate is placed inside a vacuum chamber, in which a block of the material to be deposited is also located. The source material is then heated to the point where it starts to boil and evaporate. The vacuum is required to allow the molecules to evaporate freely in the chamber, and they subsequently condense on all surfaces. This

principle is the same for all evaporation technologies, only the method used to the heat (evaporate) the source material differs. There are two popular evaporation technologies, which are e-beam evaporation and resistive evaporation each referring to the heating method. In e-beam evaporation, an electron beam is aimed at the source material causing local heating and evaporation. The material to be evaporated is in the form of single ingots if they are to be melted or in pieces if they are to be sublimated. The electron beams can be generated by thermionic emission, field electron emission or the anodic arc method. The generated electron beam is accelerated to a high kinetic energy and focused towards the ingot. When the accelerating voltage is between 20 kV – 25 kV and the beam current is a few amperes, 85% of the kinetic energy of the electrons is converted into thermal energy as the beam bombards the surface of the ingot. The surface temperature of the ingot increases resulting in the formation of a liquid melt. Although some of incident electron energy is lost in the excitation of X-rays and secondary emission, the liquid ingot material evaporates under vacuum.

2.4.3 Rapid Thermal Processing

Rapid Thermal Processing (RTP) refers to a semiconductor manufacturing process which heats semiconductor wafers to high temperatures (up to 1200 ºC or greater) on a timescale of several seconds or less. The wafers must be brought down (temperature) slow enough however, so they do not break due to thermal shock. Such rapid heating rates are attained by high intensity lamps or laser process. These processes are used for a wide variety of applications in semiconductor manufacturing including dopant activation, thermal oxidation, and metal reflow/alloying. Rapid thermal was performed on ZnO

samples with metal contacts on the films. This process is carried out to improve the contact resistance for precise device measurements or to convert Schottky contacts to Ohmic by better alloying of metal with the ZnO material through various mechanisms. The thermal annealing is always performed in N_2 environment to protect the samples from moisture and contamination. The heating is performed by a lamp while it is monitored by either a thermocouple or a pyrometer. Thermocouple is used for low-temperature ranges while pyrometer is used for higher temperatures. The sample is left in the annealing chamber until a temperature less than 150 ºC is reached.

2. 5 Sample and device characterization method

2.5.1 SEM

The scanning electron microscope (SEM) is a microscope that uses electrons instead of light to form an image. A beam of electrons is produced at the top of the microscope by an electron gun composed commonly by a Ta filament and an anode. The electron beam follows a straight vertical path through the microscope, which has to be held within a vacuum. The beam travels through electromagnetic fields and lenses, which focus the beam, like its light counterparts, down toward the sample. Once the beam hits the sample, secondary electrons, X-rays and photons are ejected from the sample. These particles are then detected and processed into an image. The scanning electron microscope has many advantages over traditional microscopes. The SEM has a large depth of field, which allows for specimens with large height contrast to be in focus at one time. The SEM also has much higher resolution, so closely spaced specimens bellow the 200nm limit of light microscopes can still be detected at much higher levels. Because the

SEM uses electromagnets rather than lenses, the researcher has much more control in the degree of magnification. All of these advantages, as well as the actual strikingly clear images, make the scanning electron microscope one of the most useful instruments in research today.

2.5.2 TEM characterization

The transmission electron microscope (TEM) uses a higher energy electron beam than an SEM (>100 kV) transmitted through a very thin sample to image and analyze the structure of materials with atomic scale resolution. The electron beam is focused with electromagnetic lenses and the image is observed on a fluorescent screen, or recorded with a digital camera. The electrons are accelerated to several hundred kV, giving them wavelengths much smaller than that of light (200kV electrons have a wavelength of 0.025Å). However, whereas the resolution of the optical microscope is limited by the wavelength of light, that of the electron microscope is limited by aberrations inherent in electromagnetic lenses, to about 1-2 Å.

Because it is almost impossible to look trough a single layer of atoms, is it unlikely that TEM images would yield images of individual atoms. Rather for high resolution TEM images that show the crystal lattice of a material it is actually the interference pattern between the transmitted and diffracted beams. This imaging mode allows us to observe planar and line defects, grain boundaries, interfaces, etc. with atomic scale resolution. The TEM has also the capability of having brightfield/darkfield imaging and diffraction pattern modes, which operate at intermediate magnification. They also provide invaluable information about the morphology, crystal phases, and defects in a material.

2.5.3 X-ray Diffraction

X-ray scattering techniques are non-destructive analytical techniques, which reveal information about the crystallographic structure, chemical composition, and physical properties of materials and thin films. The techniques are based on observing the scattered intensity of an x-ray beam hitting a sample as a function of incident and scattered angle, polarization, and wavelength or energy. X-ray diffraction techniques are based on the elastic scattering of X-rays from structures that have long range order. The experiments involve a beam of X-rays incident on the sample, which is reflected from atomic planes, producing a diffraction pattern of spots called reflections by Bragg's law of diffraction. Each reflection corresponds to one set of evenly spaced planes within the crystal. The density of electrons within the crystal is determined from the position and brightness of the various reflections observed as the crystal is gradually rotated in the X-ray beam; this density, together with supplementary data, allows the atomic positions to be inferred. For single crystals of sufficient purity and regularity, X-ray diffraction data can determine the mean positions of most atoms to within a few tenths of an Angstrom and also allows the static and dynamic disorder in those positions to be estimated. Hence, by measuring the diffraction pattern, the crystalline structure of the sample can be studied. The quality of the sample or introduction of impurities can be inferred from the FWHM of the peaks observed. The θ-2θ scans were performed on our ZnO samples using a Bruker Advanced XRD in the experiments.

2.5.4 Secondary Ion Mass Spectroscopy

Secondary ion mass spectroscopy (SIMS) is a powerful tool using which the composition or distribution of various elements in a sample can be studied. The spectroscopy typically utilizes a primary ion beam which is incident on the surface of the sample. The surface then emits material through a sputtering process, a fraction of which is in the form of secondary ions. These secondary ions are measured with a mass spectrometer to determine the quantitative elemental or isotopic composition of the surface. In this dissertation, Cameca 4f SIMS system from the Evans Analytical Group was used. The bombarded ions were analyzed with Cs^+ beam sputtering with impact energy of 14.5 keV, sample bias of –4.5 keV and a primary energy of +10 keV and negative secondary ion detection. The beam raster size is 150 μm×150 μm; and the collection area is 25 μm in diameter. Analysis was performed using high mass resolution so that the ion was mass-separated from molecular interferences that have the same nominal mass. AMPAC characterization facility from University of Central Florida was also used, where Cs or O primary beams were used.

2.5.5 Photoluminescence

Photoluminescence (PL) is an analytical technique that provides information about the optical properties of a film. A light source, such as He-Cd, Ar or Kr laser, with energy larger than the bandgap energy of the semiconductor being studied, generates electron-hole pairs within the semiconductor. The excess carriers can recombine via radiative and nonradiative recombination. Photoluminescence, the light emitted from radiative

recombination, is detected. The wavelength associated with the different recombination mechanisms is measured.

The luminescence from excitons, electrons and holes bound to each other, is observed only at low temperatures in highly pure materials. As the temperature increases, the exciton breaks up into free carriers from the thermal energy. Increasing dopant concentration also causes dissociation of excitons under local electric fields. Under these conditions, the electrons and holes recombine via the band-to-band process. Since some of the electrons may not lie at the bottom of the conduction band, their recombination and holes will produce a high energy tail in the luminescence spectrum. On the other hand, the band-to-band recombination will yield a sharp cutoff at the wavelength corresponding to the bandgap of the material. [63]

In this study, PL was measured at room and low temperature using the 325 nm line of a He-Cd laser (20 mW) as an excitation source. PL was dispersed with a 1m double monochromator and processed using time-correlated signal-photon-counting electronics. Figure 2.4 shows a schematic diagram of the photoluminescence setup in this study.

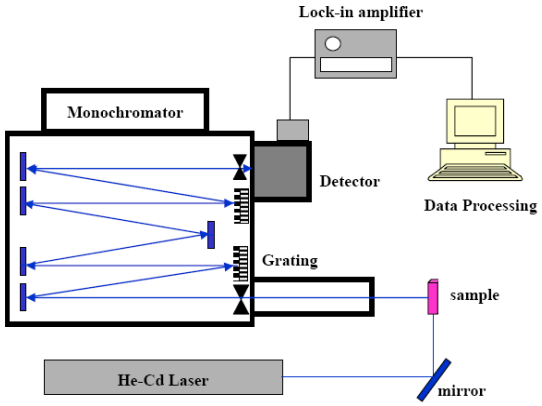

Figure 2.4. Schematic diagram of a photoluminescence measurement set-up.

2.5.6 Hall measurement

The electrical properties of a sample, such as electron and hole concentration, and their mobilities were measured using two ways: 1. A conventional Van der Pauw configuration, which holds only when the following four conditions are satisfied. i) The contacts are at the circumference of the sample; ii) the contacts are sufficiently small; iii) the sample is uniformly thick; and iv) the sample surface is singly connected. A commercial HMS3000 Hall system was utilized. 2. Hall bar configuration in a PPMS system. In the hall bar configuration, the hall resistance is measured against the magnetic field. In principle, the magnitude of the hall resistance is linearly to the magnetic field. The coefficient is depending on the carrier type and the sample geometry.

2.5.7 Electrical measurements

Current-voltage (I-V) measurements were taken to characterize the electrical properties of the contacts. These measurements are performed on a semiconductor parameter analyzer connected to a micromanipulator probe station. For vertical diodes, the input voltage will be applied to a highly conductive copper disk on which the samples were mounted on the backside with silver paste. Capacitance-Voltage (C-V) characterization involves probing of a junction at varied frequencies. From the C-V, parameters such as built-in potential of the junction and doping concentrations of material can be obtained. Measurements were carried out using Agilent 4284A precision LCR meter and were controlled by using software programmed by Labview.

2.5.8 Electroluminescence measurements

The operation of almost all optoelectronic devices is based on the creation or annihilation of electron-hole pairs. Electron-hole pair formation essentially involves raising an electron in energy from the valence band to the conduction band, thereby leaving a hole behind in the valence band. Photoluminescence involves radiative recombinations of electron-hole pairs created by injection of photons, while electroluminescence is the process of generating photon emission when the excitation of excess carriers is an electric current caused by an applied electric field.

In our experiments, we use a homemade EL system which is combined with the PL system. A function generator provides the DC current 0-200 mA for the device operation. The emission is collected and analyzed as the same way with the PL system.

2.6 Reference

[1] D.C. Look, Mater. Sci. Eng. B80, 383 (2001).

[2] National Compound Semiconductor Roadmap/Basic Material Properties: http://www.onr.navy.mil/sci_tech/information/312_electronics/ncsr/properties.asp (June 2005).

[3] D.W. Palmer, The Semiconductor Information Website, II-VI Properties: http://www.semiconductors.co.uk/propiivi5410.htm (June 2005).

[4] U. Ozgur, Y. I. Alivov, C. Liu, A. Teke, M. A. Reshchikov, S. Dogan, V. Avrutin, S. J. Cho, and H. Morkoc, J. Appl. Phys. 98, 041301 (2005).

[5] S. J. Pearton, D. P. Norton, K. Ip,Y. W. Heo, T. Steiner, Progress in Materials Science 50, 293–340 (2005).

[6] E. Ohshima, H. Ogino, I. Niikura, K. Maeda, M. Sato, M. Ito, and T. Fukuda, J. Cryst. Growth 260, 166 (2004).

[7] J. M. Ntep, S. S. Hassani, A. Lusson, A. Tromson Carli, D. Ballutaud, G. Didier, and R. Triboulet, J. Cryst. Growth 207, 30 (1999).

[8] D.C. Look, D.C. Reynolds, J.W. Hemsky, R.L. Jones, and J.R. Sizelove, Appl. Phys. Lett. 75, 811 (1999).

[9] Y. Yan, P. Liu, M. J. Romero and M. M. Al-Jassim, J. Appl. Phys. 93, 4807 (2003).

[10] J. Lao, J. Huang, D. Banerjee, S.-H. Jo, D. Wang, J. Wen, D.M. Steeves, B.R. Kimball, W. Porter, R.A. Farrer, T. Baldacchini, J.T. Fourkas ans Z. Ren, Proc. SPIE Int. Soc. Opt. Eng. 5219, 99 (2003).

[11] H. T. Ng, J. Li, M. K. Smith, P. Nguyen, A. Cassel, J. Han and M. Meyyappan, Science 300, 1249 (2003)

[12] L. Luo, Y. Zhang, S. S. Mao and L. Lin, Sensors and Actuators A, 127, 201 (2006)

[13] S. Chang, H. Hung, Y. Lin, C. Huang, Y. Tseng and I Chen, Nanotechnology, 4, 649 (2005)

[14] S. Ren, Y. F. Bai, J. Chen, S. Z. Deng, N. S. Xu, Q. B. Wu and S. Yang, Materials Lett. 61, 666 (2007)

[15] Y. Fang, Q. Pang, X. Wen, J. Wang and S. Yang, Small, 2, 612 (2006)

[16] J. C. Phillips, Bonds and Bands in Semiconductors, Academic, New York, (1973).

[17] D. R. Lide (Ed.), CRC Handbook of Chemistry and Physics, 73rd Edition, CRC Press, New York, (1992).

[18] T. Kogure, Y. Bando, J. Electron Microsc. 47, 7903 (1993).

[19] A. B. M. A. Ashrafi, A. Ueta, A. Avramescu, H. Kumano, I. Suemune, Y. W. Ok, T. Y. Seong, Appl. Phys. Lett. 76, 550 (2000).

[20] S. K. Kim, S. Y. Seong, C. R. Cho, Appl. Phys. Lett. 82, 562 (2003).

[21] C. H. Bates,W. B. White, R. Roy, Science 137, 993 (1962).

[22] J. E. Jaffe, J. A. Snyder, Z. Lin, A. C. Hess, Phys. Rev. B 62, 1660 (2000).

[23] T. Makino, C. H. Chia, N. T. Tuan, H. D. Sun, Y. Segawa, M. Kawasaki, A. Ohtomo, K. Tamura, H. Koinuma, Appl. Phys. Lett. 77, 975 (2000).

[24] K. Ogata, K. Koike, T. Tanite, T. Komuro, F.Yan, S. Sasa, M. Inoue, M.Yano, J. Cryst. Growth 251, 623 (2003).

[25] T. Makino, Y. Segawa, M. Kawasaki, A. Ohtomo, R. Shiroki, K. Tamura, T. Yasuda, H. Koinuma, Appl. Phys. Lett. 78, 1237 (2001).

[26] L. K. Wang, Z. G. Ju, J. Y. Zhang, J. Zheng, D. Z. Shen, B. Yao, D. X. Zhao, Z. Z. Zhang, B. H. Li and C. X. Shan, Appl. Phys. Lett. 95, 131113 (2009)

[27] Z. P. Wei, B. Yao, Z. Z. Zhang, Y. M. Lu, D. Z. Shen, B. H. Li, X. H. Wang, J. Y. Zhang, D. X. Zhao, X. W. Fan and Z. K. Tang, Appl. Phys. Lett. 89, 102104 (2006)

[28] L. Bergman, J. L. Morrison, X. Chen, J. Husu and H. Hoeck, Appl. Phys. Lett. 88, 023103 (2006)

[29] C. Y. Liu, H. Y. Xu, L. Wang, X. H. Li and Y. C. Liu, J. Appl. Phys. 106, 073518 (2009)

[30] H. C. Jeon, S. H. Park, S. J. Lee, T. W. Kang and T. F. George, Appl. Phys. Lett. 96, 101113 (2010)

[31] J. W. Mares, M. Falanga, A. V. Thompson, A. Osinsky, J. Q. Xie, B. Hertog, A. Dabiran, P. P. Chow, S. Karpov, and W. V. Schoenfeld, J. Appl. Phys. 104, 093107 (2008)

[32] A. V. Thompson, C. Boutwell, J. W. Mares, W. V. Schoenfeld, A. Osinsky, B. Hertog, J. Q. Xie, S. J. Pearton, and D. P. Norton, Appl. Phys. Lett. 91, 201921 (2007)

[33] H. J. Ko, Y. F. Chen, S. K. Hong, H. Wenisch, T. Yao, and D. C. Look, Appl. Phys. Lett. 77, 3761 (2000).

[34] T. Minami, H. Nanto, and S. Takata, Jpn. J. Appl. Phys. Part 2 24, L781 (1984).

[35] T. Minami, H. Sato, H. Nanto, and S. Takata, Jpn. J. Appl. Phys. Part 2 25, L776 (1985).

[36] P. Souletie, S. Bethke, B. W. Wessels, and H. Pan, J. Cryst. Growth 86, 248 (1988).

[37] Kyoung-Kook Kim, Hyun-Sik Kim, Dae-Kue Hwang, Jae-Hong Lim, and Seong-Ju Park, Appl. Phys. Lett. 83, 63 (2003).

[38] C. G. Van de Walle, Phys. Rev. Lett., 85, 1012 (2000).

[39] M. D. McCluskey, S. J. Simpson, and K. G. Lynn, Appl. Phys. Lett. 81, 3807 (2002).

[40] K. K. Kim, H. S. Kim, D.-K. Hwang, J.-H. Lim, and S.-J. Park, Appl. Phys. Lett. 83, 63 (2003)

[41] Y. R. Ryu, T. S. Lee, and H. W. White, Appl. Phys. Lett. 83, 87 (2003),

[42] S. Limpijumnong, S. B. Zhang, Su-Huai Wei, and C. H. Park, Phys. Rev. Lett. 92, 155504 (2004),

[43] H. S. Kang, B. D. Ahn, J. H. Kim, G. H. Kim, S. H. Lim, H. W. Chang, and S. Y. Lee, Appl. Phys. Lett. 88, 202108 (2006).

[44] C. Klingshirn, Phys. Stat. Sol. (b) 244, No. 9, 3027– 3073 (2007).

[45] D. C. Reynolds, D. C. Look, B. Jogai, C. W. Litton, G. Cantwell, and W. C. Harsch, Phys. Rev. B, 60, 2340 (1999).

[46] Walter R.L. Lambrecht, Anna V. Rodina, Sukit Limpijumnong, B. Segall, and Bruno K. Meyer, Phys. Rev. B, 65, 075207 (2002).

[47] F. X. Xiu, Z. Yang, L. J. Mandalapu, D. T. Zhao, and J. L. Liu, Appl. Phys. Lett. 87, 252102 (2005)

[48] F. X. Xiu, Z. Yang, L. J. Mandalapu, D. T. Zhao, J. L. Liu, and W. P. Beyermann, Appl. Phys. Lett. 87, 152101 (2005)

[49] P. Fons, K. Iwata, S. Niki, A. Yamada, and K. Matsubara, J. Cryst. Growth 201–202, 627 (1999).

[50] Y. Chen, D. M. Bagnall, H.-J. Koh, K. T. Park, K. Hiraga, Z. Q. Zhu, and T. Yao, J. Appl. Phys. 84, 3912 (1998).

[51] M. Kasuga and M. Mochizuki, J. Cryst. Growth 54, 185 (1981).

[52] V. Srikant, V. Sergo, and D. R. Clarke, Appl. Phys. Lett. 16, 439 (1995).

[53] E. M. Kaidashev, M. Lorenz, H. von Wenckstern, A. Rahm, H.-C. Semmelhack, K.-H. Han, G. Benndorf, C. Bundesmann, H. Hochmuth, and M. Grundmann, Appl. Phys. Lett. 82, 3901 (2003).

[54] R. D. Vispute, V. Talyansky, Z. Trajanovic, S. Choopun, M. Downes, R. P. Sharma, T. Venkatesan, M. C. Woods, R. T. Lareau, K. A. Jones, and A. A. Iliadis, Appl. Phys. Lett. 70, 2735 (1997).

[55]J. F. Muth, R. M. Kolbas, A. K. Sharma, S. Oktyabrsky, and J. Narayan, J. Appl. Phys. 85, 7884 (1999)

[56] V. Craciun, J. Elders, J. G. E. Gardeniers, and Ian W. Boyd, Appl. Phys. Lett. 65, 2963 (1994)

[57] X. W. Sun and H. S. Kwok, J. Appl. Phys. 86, 408 (1999)

[58] P. F. Carcia, R. S. McLean, and M. H. Reilly, Appl. Phys. Lett. 88, 123509 (2006)

[59] S. J. Lim, Soon-ju Kwon, Hyungjun Kim, and Jin-Seong Park, Appl. Phys. Lett. 91, 183517 (2007)

[60] J. Nause and B. Nemeth, Semicond. Sci. Technol. 20, S45 (2005).

[61] K. Ellmer, J. of Phys. D Appl. Phys. 33 (4): R17-R32 (2000).

[62] J. G. E. Gardeniers, Z. M. Rittersma, and G. J. Burger, J. Appl. Phys. 83, 7844 (1998).

[63] C.R. Brundle, C.A. Evans, Jr. and S. Wilson, Encyclopedia of Materials Characterization, Butterworth Heinemann, Stoneham, MA (1992).

Chapter III ZnO homojunction light emitting diode

3. 1. Motivation of the ZnO homojunction LED

ZnO is considered to be a promising material for ultraviolet (UV) light emitting diodes (LEDs) and laser diodes (LDs) due to its direct band gap of 3.37 eV and large exciton binding energy of 60 meV.[1-3] Nevertheless, unlike n-type ZnO,[4] reliable p-type doping is difficult to achieve due to the possibility of holes getting compensated by the intrinsic donors such as zinc interstitials and oxygen vacancies. Therefore, previous efforts on ZnO p-n junctions are mostly made from n-type ZnO and other p-type semiconductors such as Si, SiC, GaN, $SrCu_2O_2$ and so on.[5-7] The benefit of making those heterojunction LEDs is that it is easy to obtain a device, however, the chemical and crystallographic differences between ZnO and dissimilar materials give rise to the formation of interfacial defects, which makes negative impact on optical and electrical properties of diodes. There are three main disadvantages of heterojunction structure.

First, lattice mismatch, chemical and crystallographic difference between two materials give rise to a large amount of dislocations at the interface. The defects bring energy levels in between the conduction band and the valence band, either working as non-radiative emission centers or contributing to deep level emissions. The consequences reduce the internal efficiency and enhance the unexpected intermediate recombination.

Second, the electrical band structure offset at interface forms abrupt barriers, which block carrier transportation at one way or both ways. For a p-n junction diode, the recombination region is very close to the interface, so the non-efficient recombination is expected with this structure.

Third, different thermal properties of two materials lead to thermal unreliability for a working device. The efficiency is reduced by the expansion of deformation with different thermal expansion coefficients.

In general, one expects to develop the p-n junction LED with a homojunction structure. Although ZnO p-type doping is a challenge, several groups have tried different dopants such as Cu, Li, Ag, N, P, Sb, As and some recently reported light emitting diodes based on ZnO p-n homojunction structures.[8-13] Due to poor crystalline quality, all of those devices, however, yield deep level related emissions with much larger intensity than near band edge emissions. The fundamental reasons are radiative recombination associated with high-density in-active dopants, high-density Zn or O point defects, and poor material quality. To resolve some of these problems and achieve dominant near band edge emissions over deep-level emissions for possible practical applications, in this chapter, we report our fabrication and characterization of Sb-doped p-type ZnO/Ga-doped n-type ZnO closely packed columnar structure LEDs on Si that show dominant UV emissions at room temperature. The reason of insignificant deep-level emissions in our devices is discussed.

3. 2 Sample growth and device fabrication procedures

ZnO p-n junction was grown on n-type Si (100) substrate (1-20 Ω·cm) using molecular beam epitaxy (MBE) system. Typical cleaning procedure for Si substrates includes cleaning in boiling Piranha solution (H_2O_2:H_2SO_4 =3:5) for 1 min and followed by aqueous HF solution (HF:H_2O=1:10) for 1 min to hydrogenate the substrate surface. The substrate was then introduced into growth chamber and thermally cleaned by

annealing at 800 ˚C in vacuum for 20 minutes. Further, the Si substrates were thermally cleaned at 650 ˚C for 10 min to disassociate hydrogen bonds, leaving a fresh Si surface for subsequent growth after transferring into the vacuum chamber.

Oxygen source is pure O_2 (5N) gas and a radio-frequency plasma source was used to generate oxygen plasma. A thin magnesium oxide (MgO) buffer layer was deposited at 350 ºC to reduce the lattice mismatch between Si and ZnO, followed by 410nm Ga-doped n-ZnO and 410nm Sb-doped p-ZnO. The p-n junction diodes with defined mesa size 800μm×800μm were fabricated by employing standard photolithography techniques. Au/NiO (500/30 nm) and Au/Ti (200/30 nm) were then deposited on p-type ZnO and n-type ZnO, respectively by lift-off process. The contacts were annealed at 550 ^{o}C for Au/NiO and 850 ^{o}C for Au/Ti respectively to form Ohmic contact. The devices were packaged on TO5 cans using conductive epoxy resin and annealed at 150 ^{o}C for 60 mins. Figure 3.1 shows the schematic structure of the ZnO homojunction device.

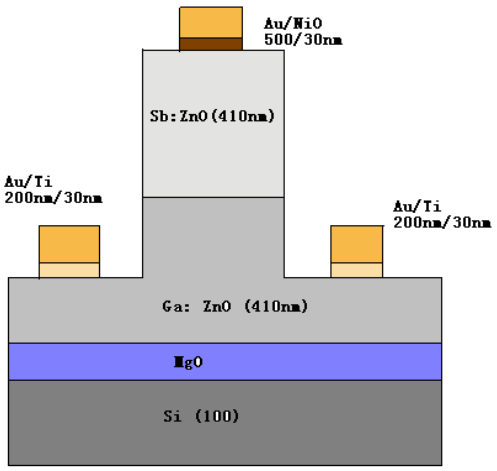

Figure 3.1 Device structure of the ZnO homojunction LED

3.3. Characterization of ZnO homojunction sample

3.3.1 Material characterization

X-ray diffraction (XRD) θ/2θ scans show that the diode film grows preferentially along the c-direction of the ZnO Wurtzite lattice (Fig.3.2(a)). Surface morphology and cross-section of ZnO film were studied by scanning electron microscope (SEM). Fig. 3.2 (b) shows the top-view image of the ZnO film on Si substrate. It is evident that ZnO grains with in-plane size from 100nm to 400nm are formed, which is the typical result of oriented nucleation process due to the large lattice mismatch between ZnO and Si substrate.[14] Large lattice mismatch between ZnO and Si substrate is released by formation of column planar defects. Within each column, however, high epitaxial crystalline quality is expected. Fig. 3.2 (c) is the image in the cross-section configuration of the film, which clearly presents nano-columnar structures.

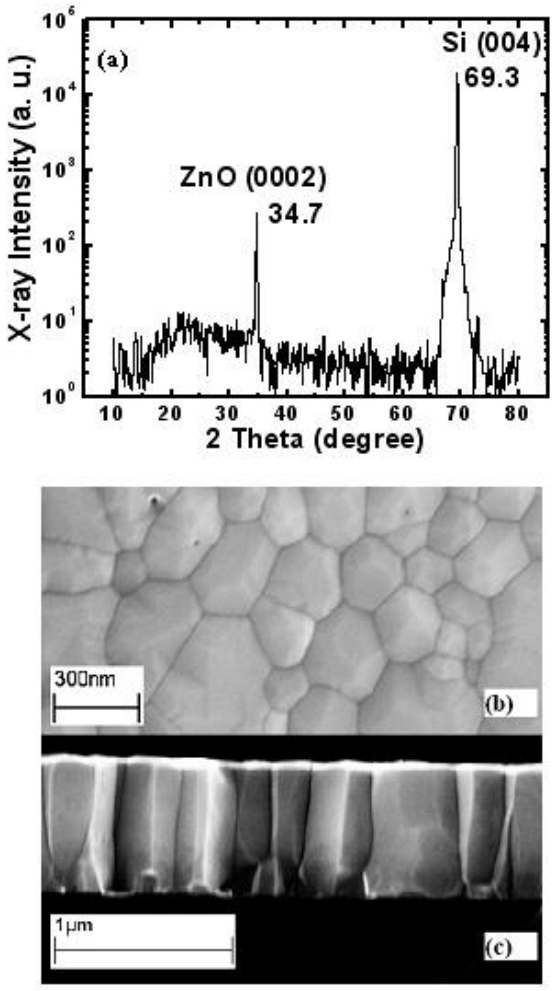

Figure 3.2(a) XRD spectrum of ZnO p-n junction on Si (100) substrate, **(b)** SEM image of sample surface, and **(c)** Cross-sectional SEM image of the ZnO diode.

The elemental distribution of Zn, O, Sb, Ga and Si was obtained by performing secondary ion mass spectroscopy (SIMS) measurements, where Cs ion beam was used, as shown in Fig. 3.3. Dominant distribution of Sb and Ga dopants are in p-type and n-type layers, respectively, leading to relatively sharp p-n junction interface. The hole concentration in p type layer is about an order smaller than the electron concentration in n

type layer, as deducted from Fig. 3.3. The depletion region will be mostly on the p type side thereby, which determines the recombination area.

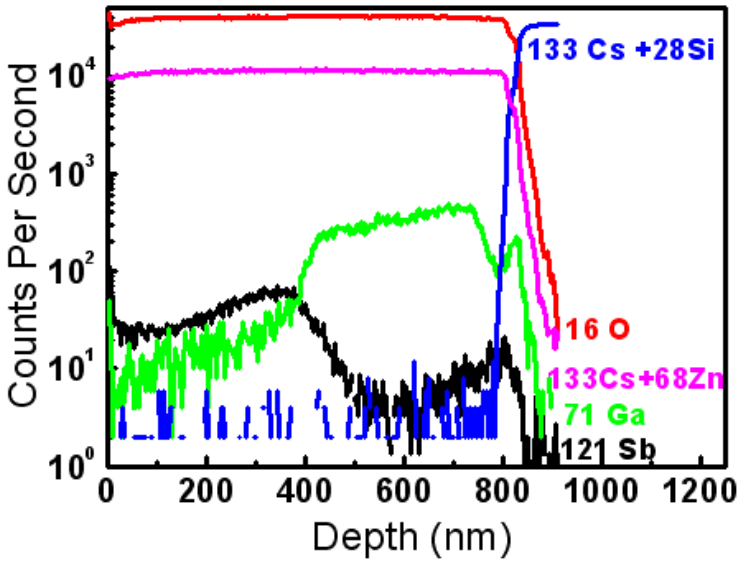

Figure 3.3 SIMS result of ZnO p-n junction on Si (100) substrate. The elemental profiles of Sb, Ga dopants, Zn, O and Si substrate can be seen.

3.3.2 Device characterization I-V and C-V

I-V characteristics were measured using Agilent 4155C semiconductor parameter analyzer and Signatone probe station. The specific contact resistivity of p-layer was calculated to be 9.3×10^{-5} $\Omega\cdot cm^2$. C-V characteristics were measured using Agilent 4155C semiconductor parameter analyzer and Agilent 4284A precision LCR meter. Fig 3.4 shows I-V characteristics of the p-n junction and the right inset is C-V characteristics. The diode shows fairly good rectification behavior with a threshold voltage of about 2.5 V. These results suggest that we have formed ZnO p-n junction diodes.

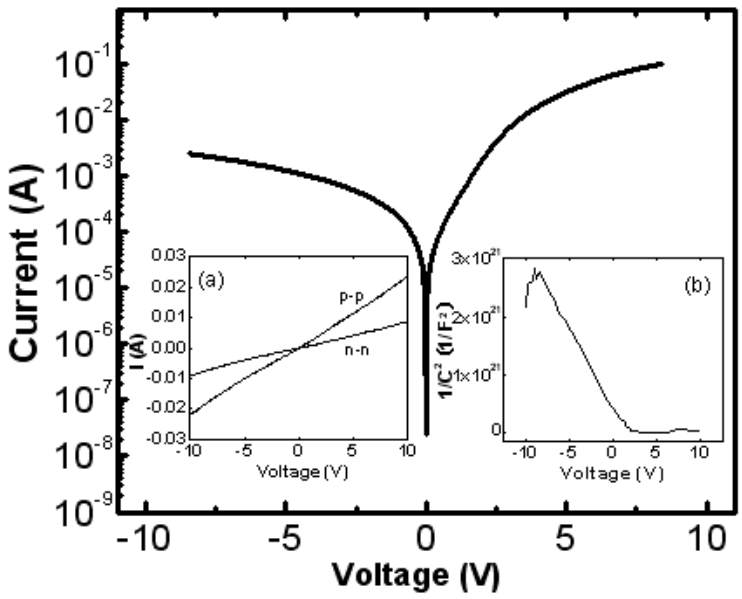

Figure 3.4 I-V characteristics of the p-n homojunction diode, showing typical rectifying characteristics. The left inset (a) shows the I-V curve of both n-type and p-type contacts. The right inset (b) shows $1/C^2$-V characteristics confirming p-n junction with built-in potential of about 2.5 V.

3.3.3 EL characterization at room temperature

Electroluminescence (EL) measurements were performed using an Oriel monochromator and photomultiplier tube at room temperature. The diode was biased under DC forward voltages. Figure 3.5 shows the EL spectra obtained at different injection current. Near band edge emission at 3.2 eV started to appear when the current is 60 mA. Afterwards, the intensity of this emission increases as the injection current increases from 60 mA to 100 mA. Moreover, the intensity of this emission peak increases evidently from 60 mA to 80 mA while it changes less significantly from 80 mA to 100 mA, which is due to the heat effect as a result of the increasing current through the diode. Several other deep level emission peaks near 475 nm (green band) and 610 nm (yellow

band) were routinely reported in the literatures, related to O vacancy and O interstitial in n-type and p-type ZnO, respectively.[15-17] In this case, experimental results show that UV near band edge emissions are always dominant in the emission spectra while defect-related yellow and green band emissions are very weak.

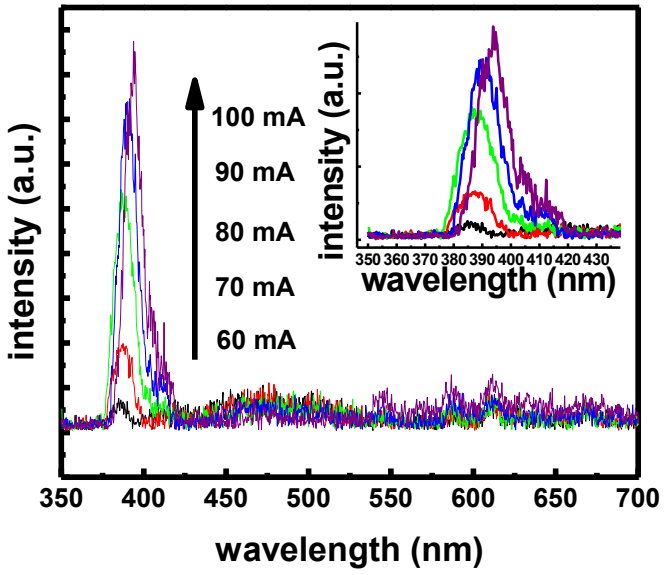

Figure 3.5 Electroluminescence spectra of p-n ZnO diode at room temperature, with increasing injection current from 60 mA to 100 mA. The inset is magnified spectrum at UV region.

Moreover, the dominance of UV emission is much clearer at higher injection currents. While injection current increases from 60 mA to 100 mA, the UV emission peak also slightly redshifts from 385nm to 393nm, as shown in the inset of Fig.3.5. This is typical in a radiative combination process for direct band gap material because heat induced by increased injection current will decrease its effective band gap.[18] Fitting the

experimental result by using Varshni's equation: $E_g(T)=E_0-\alpha\times T^2/(T+\beta)$, and assuming device temperature is increased mainly by resistance heat, since the resistance in this diode is large. So we have $(T-300K)\sim I^2$, we obtain α,β to be 8.2×10^{-4} and 1060 respectively, and E_g at 300K for ZnO to be 3.25 eV. α and β values are consistent with what were reported. [19,20]

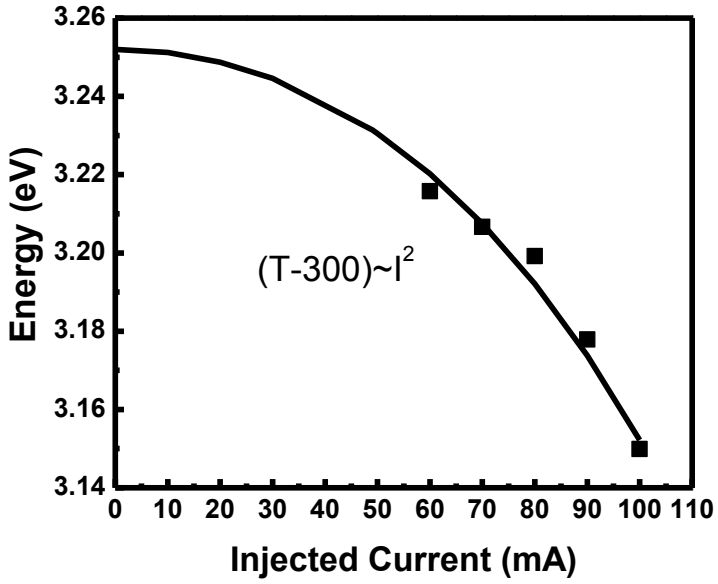

Figure 3.6 EL peak positions under different injection currents, with a fitting curve using Vashini's equation

The integrated intensity with different injection currents is plotted in Fig 3.7. The result can be fitted to the power law, where $L=cI^p$. The fitting result gave P=1, indicating the linear dependence on the injection current. The linear relation is a typical result for LED devices with conventional GaAs/AlGaAs, GaN/InGaN LEDs. The linear relation indicates that every injected carrier leads to the emission of a photon. [21]

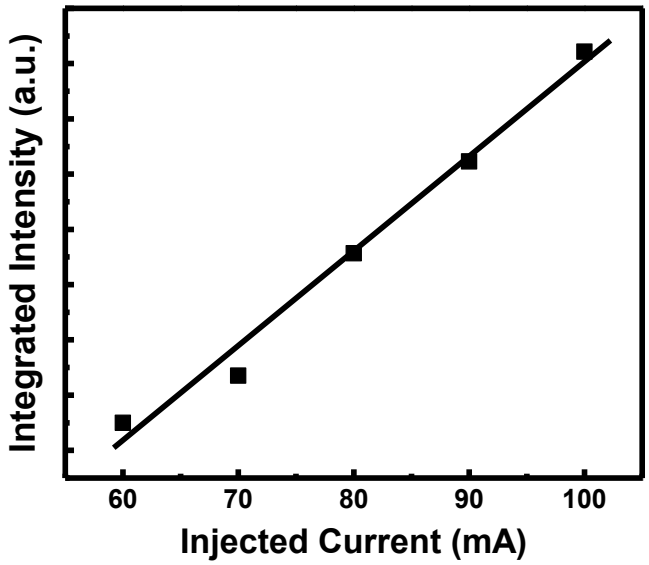

Figure 3.7 EL Integrated intensity at different injection current from 60 mA to 100 mA at room temperature

3.3.4 EL characterization at low temperature

Due to heat effect, the output power of this homojunction LED is still very low, compared to commercial product. To further investigate the LED characteristics, low temperature EL measurement was performed at 17K background, as shown in Fig 3.8. In Fig. 3.8, EL spectra obtained at various input injection currents starting from 5 mA to 170 mA are shown. The redshift from 5 mA to 110 mA is slight, while the redshift from 110 mA to 170 mA is significant. Not only the peak position shifted, but also the intensity decreased, with strong efficiency drop accordingly.

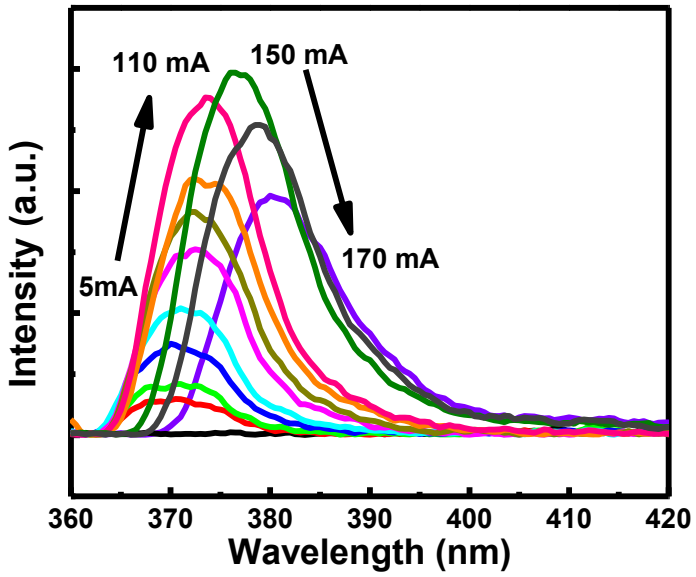

Figure 3.8 Electroluminescence spectra of p-n ZnO diode at room temperature, with increasing injection current from 5 mA to 170 mA.

Fig.3.9 shows the emission peak position with different injection currents. The solid line is a fitting by using Varshni's equation: $E_g(T)=E_0-\alpha\times T^2/(T+\beta)$ and the parameters obtained from room temperature results. It shows good match with low temperature data as well, and it proves that the heat is mainly from resistor heat due to the high junction resistance.

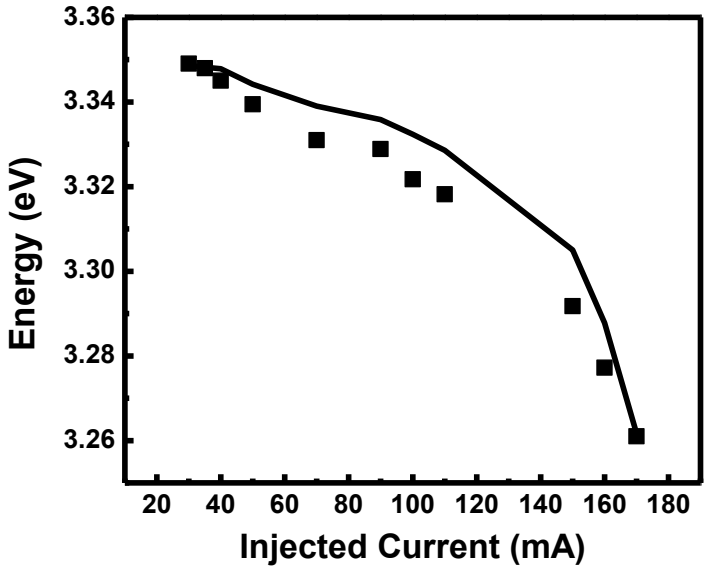

Figure 3.9 EL peak positions under different injection currents, with a fitting curve using Varshni's equation

In Fig.3.10, the light output intensity versus current characteristic of the diode is shown. The integrated output power undergoes an ascent trend and then decreases after 150 mA. The results show that after 150 mA, the efficiency decreases intensively due to heat effect.

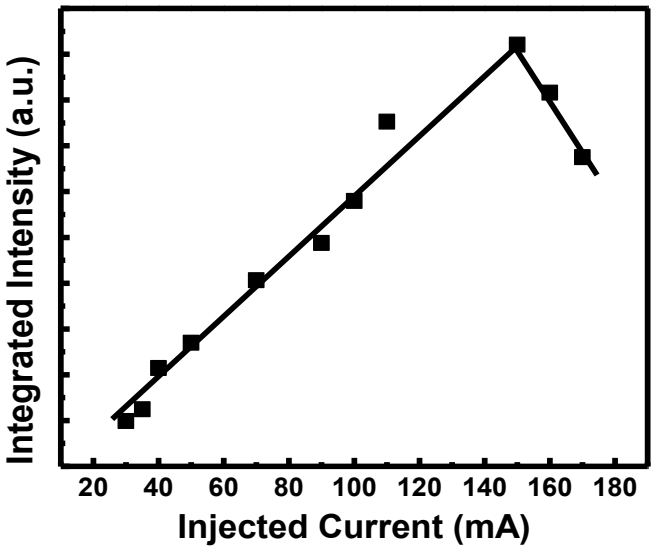

Figure 3.10 EL Integrated intensity at different injection current from 60 mA to 100 mA at 17 K background

3.3.5 LED efficiency decay

LED failure is the gradual lowering process of light output and loss of efficiency. To test the lifetime of this homojunction LED, time dependent output power evolution was plotted in Fig.3.11. The lifetime of this device is relatively short, the efficiency loses 25% in 660 seconds. There are two principal reasons for the efficiency degradation. First, reduction of internal quantum efficiency is caused by different temperature dependence of the radiative and non-radiative recombination rates. Second, the carrier leakage from the active region is enhanced by the high current density and temperature.

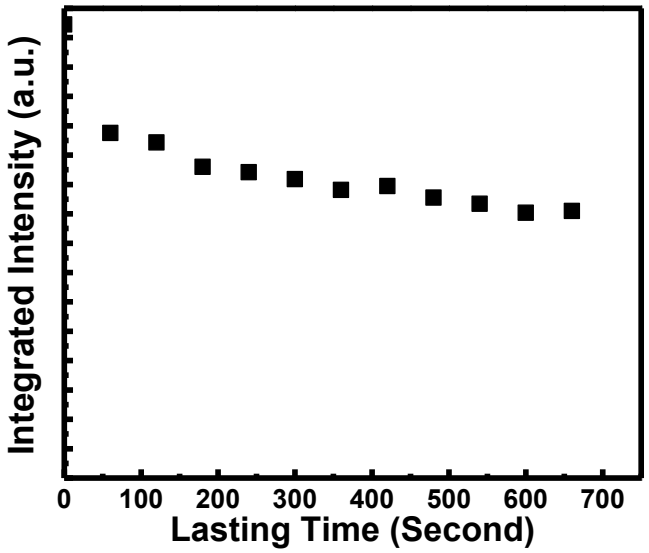

Figure 3.11 EL integrated intensity measured at different decay time

3.4 Discussion

To understand the dominant UV emissions, we realized that the "film" consists of a great deal of vertical nano columns, which connect closely to each other. Therefore, the whole structure is a collection of packed ZnO p-n homojunction columns and the detected electroluminescence spectrum is a sum of emissions from each one of these columns. The stress from the lattice mismatch between ZnO and Si substrate is released by the formation of these columnar structures, whose side walls terminate a great deal of threading dislocations generated at column/substrate interface.

With lower dislocation density in the upper diode portion of each column, non-radiative recombinations are reduced and UV near band edge emission is dominant. Deep-level radiative yellow/green band recombinations, which were routinely observed

in other reported ZnO LEDs, are also reduced. This is also verified in the PL spectrum where no visible emissions are seen. Since the yellow/green band emissions are associated with oxygen interstitial/vacancy point defects, respectively [15-17], our results suggest that ZnO on Si can achieve insignificant amount of point defects via the formation of columnar structures under appropriate growth conditions. The output power of this LED is estimated to be only 1nW at drive current of 100mA, calibrated by a commercial GaN based UV LED using Ocean Optics integrating sphere. The low output is due to a large amount of defects existing in this structure, contributing to phonon-assisted non-radiative recombinations. To improve the efficiency, ZnO pn junctions with higher crystal quality are in progress.

3.5 Conclusion

UV ZnO light-emitting diode on Si (100) substrate has been realized. Reliable p-type ZnO is formed and microscopically the p-n homojunction consists of column nanostructures. Au/NiO and Au/Ti make good Ohmic contacts to p-type and n-type portions of the ZnO nano columns for the formation of LED devices. I-V and C-V measurements show good rectification behavior and EL experiments demonstrate dominant UV emissions, owing to better p-type quality. LED performance was characterized at both room temperature and 17 K, showing that emission peak redshift and efficiency drop were induced by heat.

3.6 Reference:

[1] S. J. Pearton, D. P. Norton, K. Ip, Y. W. Heo, and T. Steiner, J. Vac. Sci. Technol. B 22, 932 (2004).

[2] D. C. Look, Mater. Sci. Eng., B 80, 383 (2001).

[3] D. C. Look, B. Claflin, Y. I. Alivov, and S. J. Park, Phys. Status Solidi A 201, 2203 (2004).

[4] S. B. Zhang, S. H. Wei, and A. Zunger, Phys. Rev. B 63, 075205 (2001)

[5] H. Ohta, M. Orita, M. Hirano, H. Hosono, Appl. Phys. Lett. 77,475 (2000),

[6] Y. I. Alivov, J. E. V. Nostrand, D. C. Look, M. V. Chukichev, B. M. Ataev, Appl. Phys. Lett. 83, 2943 (2003).

[7] Ya. I. Alivov, U. Ozgur, S. Dogan, D. Johnstone, V. Avrutin, N. Onojima, C. Liu, J. Xie, Q. Fan, and H. Morkoç, Appl. Phys. Lett. 86, 241108 (2005)

[8] A. Tsukazaki, A. Ohtomo, T. Onuma, M. Ohtani, T. Makino, M. Sumiya, K. Ohtani, S. F. Chichibu, S. Fuke, Y. Segawa, H. Ohno, H. Koinuma, M. Kawasaki, Nat. Mater, 4, 42 (2005).

[9]W. Liu, S. L. Gu, J. D. Ye, S. M. Zhu, S. M. Liu, X. Zhou, R. Zhang,Y. Shi, and Y. D. Zheng, Y. Hang, C. L. Zhang, Appl. Phys. Lett. 88, 092101 (2006)

[10] J. C. Sun, J. Z. Zhao, H. W. Liang, J. M. Bian, L. Z. Hu, H. Q. Zhang, X. P. Liang, W. F. Liu, and G. T. Du, Appl. Phys. Lett. 90,121128 (2007)

[11] J. H. Lim, C. K. Kang, K. K. Kim, I. K. Park, D. K. Hwang, and S. J. Park, Adv. Mater. 18, 2720 (2006).

[12] F. X. Xiu, Z. Yang, L. J. Mandalapu, D. T. Zhao, J. L. Liu, and W. P. Beyermann, Appl. Phys. Lett. 87, 152101 (2005)

[13] S. Chu, J. H. Lim, L. J. Mandalapu, Z. Yang, L. Li, and J. L. Liu, Appl. Phys. Lett. 92,152103 (2008)

[14] J. W. Shin, J. Y. Lee, Y. S. No, T. W. Kim, and W. K. Choi, J. Appl. Phys. 100, 013526 (2006).

[15] X. L. Wu, G. G. Siu, C. L. Fu, and H. C. Ong, Appl. Phys. Lett. 78, 2285 (2001)

[16] S. A. Studenikin, N. Golego, M. Cocivera, J. Appl. Phys., 84,2287 (1999)

[17] Z. Z. Ye, J. G. Lu, Y. Z. Zhang, Y. J. Zeng, L. L. Chen, F. Zhuge, G. D. Yuan, H. P. He,L. P. Zhu, J. Y. Huang, and B. H. Zhao, Appl. Phys. Lett. 91,113503 (2007)

[18] D. W. Hamby, D. A. Lucca, M. J. Klopfstein, and G. Cantwell, J. Appl. Phys. 93,3214 (2003)

[19] B. Cao, W. Cai, and H. Zeng, Appl. Phys. Lett. 88, 161101 (2006)

[20] H. J. Ko, Y. F. Chen, Z. Zhu, I. Kobayashi, and H. Uchiki, Appl. Phys. Lett. 76, 1905 (2000)

[21] H. Kressel and J. R. Butler, Semiconductor Lasers and Heterojunction LEDs _Academic, Orlando, FL, 1977_, p. 218.

Chapter IV ZnO double heterojunction LED

4.1 Motivation of double heterojunction design

Our group successfully developed a process to produce reliable p-type ZnO layers on Si with good optical properties by Sb doping. [1,2] We also successfully developed good Ohmic contacts to n- and p-type ZnO films, which showed linear current-voltage (I-V) characteristics with low specific contact resistances.[3,4] We reported a p-n homojunction ZnO LED with Sb doped p-type layer grown on Si (100) substrate by Molecular Beam Epitaxy (MBE).[5] The device produced a fairly good current rectifying behavior with an EL emission peak at 380 nm. The stress from the lattice mismatch between ZnO and Si substrate is released by the formation of ZnO columnar structures with grain size from 100 nm to 400 nm, whose side walls terminate a great deal of threading dislocations generated at column/substrate interface. With lower dislocation density in the upper diode portion of each column, non-radiative recombinations are reduced and UV near band edge emission is dominant.

The simplest type of p-n LED design is the first step and is no longer used in current LED technology since there are some drawbacks which could lower the efficiency in the lighting and illumination applications.[6] First, electron injection into the p-type region is desired for achieving high internal quantum efficiency, therefore, a low injection level of holes into the n-region is required. The lifetimes derived from the bimolecular rate equation show that the radiative rate increases with the free-carrier concentration for both the low excitation limit as well as the high excitation limit.[7] It is therefore important that the region in which recombination occurs has a high carrier

concentration. Double heterojunction is alternative way to achieve such high carrier concentrations. Second, self-absorption of the generated light is high due to the entire structure possesses same composition; this reduces the light extraction efficiency.[8] Third, the radiative recombination in such LEDs is monomolecular, so that only increasing the doping can increase the emission rate.[9,10]

A double heterostructure (DH) consists of the active region in which recombination occurs and two confinement layers cladding the active region. A double heterostructure LED structure is shown schematically in Fig.4.1. The two cladding or confinement layers have a larger bandgap than the active region. If the bandgap difference between the active and the confinement regions is ΔE_g, then the band discontinuities occurring in the conduction and valence bands follow the relation.

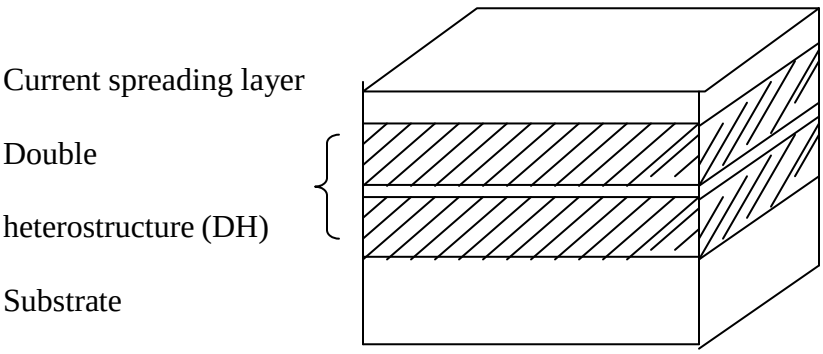

Figure 4.1 Illustration of a double heterostructure consisting of a bulk or quantum well active region and two confinement layers.

Both band discontinuities, ΔE_c and ΔE_v, should be much larger than kT in order to avoid carrier escape from the active region into the confinement regions. [11,12] The effect of a double heterostructure on the carrier concentration is illustrated schematically

in Fig.4.2. In the case of a homojunction, carriers diffuse to the adjoining side of the junction under forward bias conditions. Minority carriers are distributed over the electron and hole diffusion lengths as illustrated.

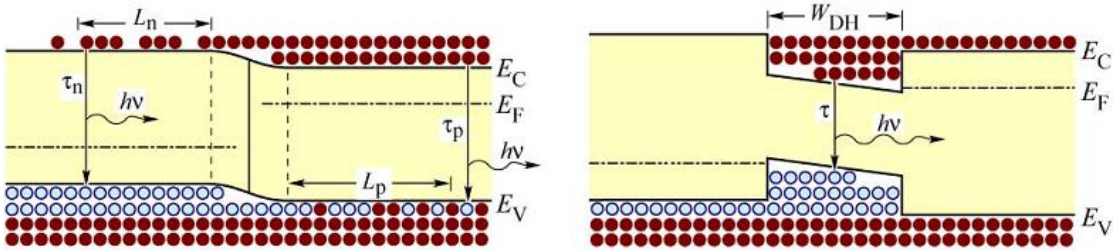

(**a) homojunction under forward bias (b) heterojunction under forward bias**

Figure. 4.2 Free carrier distribution in (a) a homojunction and (b) a heterojunction under forward bias conditions.

The wide distribution of carriers and the correspondingly low carrier concentration (particularly towards the end of the diffusion tail) can be avoided by the employment of double heterostructures. Carriers are confined to the active region, as shown in Fig. 4.2(b), as long as the barrier heights are much higher than the thermal energy kT. Today virtually all high efficiency LEDs use double heterostructure designs, like III-V nitride.

For ZnO based LEDs, a larger band gap barrier can be realized by incorporation of Mg into ZnO. However, p-type doping for (Mg,Zn)O films is really hard to be obtained,[13,14] so (Mg,Zn)O films were inserted in the n-type ZnO layer as energy barrier layers to confine the carrier recombination process to the high-quality n-type ZnO layer.[15] Fig.4.3 shows band diagram of the ZnO LED with $Mg_{0.54}Zn_{0.46}O$ layers.

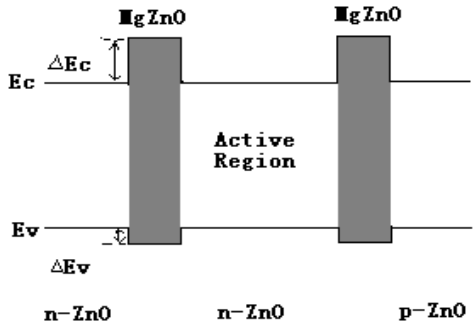

Figure. 4.3 Band diagram of ZnO based LED with $Mg_{0.54}Zn_{0.46}O$ barrier layers.

4.2 Structure growth and device fabrication

In our experiments, ZnO double heterojunction was grown on n-type Si (100) substrate (1-20 Ω·cm) using MBE system. A thin magnesium oxide (MgO) buffer layer was deposited at 350 ºC to reduce the lattice mismatch between Si and ZnO, followed by 450nm Ga-doped n-ZnO at 550 ºC. A thin MgZnO layer of about 1.5 nm was then deposited, followed by a 100 nm thick intrinsic ZnO, and on top is another 1.5 nm thick MgZnO layer. Then the temperature was increased to 600 ºC to grow 450nm Sb-doped p-ZnO. This diode sample with defined mesa size 800μm×800μm was fabricated by employing standard photolithography techniques with HCl etchant. Au/Ni (200/10 nm) and Au/Ti (200/10 nm) were then deposited on p-type ZnO and n-type ZnO, respectively by lift-off process. The contacts were annealed at 800 ^{o}C for Au/Ni and 700 ^{o}C for Au/Ti respectively to form Ohmic contact. The device structure is shown in Fig.4.4. The device was packaged onto TO5 can using conductive epoxy resin.

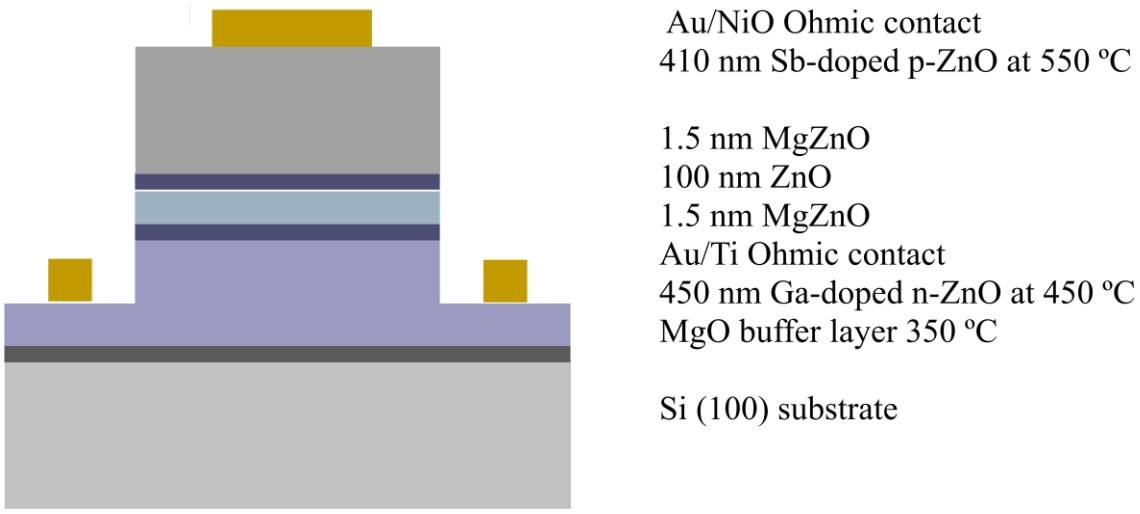

Figure 4.4 Device structure of the ZnO double heterojunction LED

4.3 Device characterization

XRD θ/2θ scans show that the diode film grows preferentially along the c-direction of the ZnO Wurtzite lattice in Fig. 4.5.

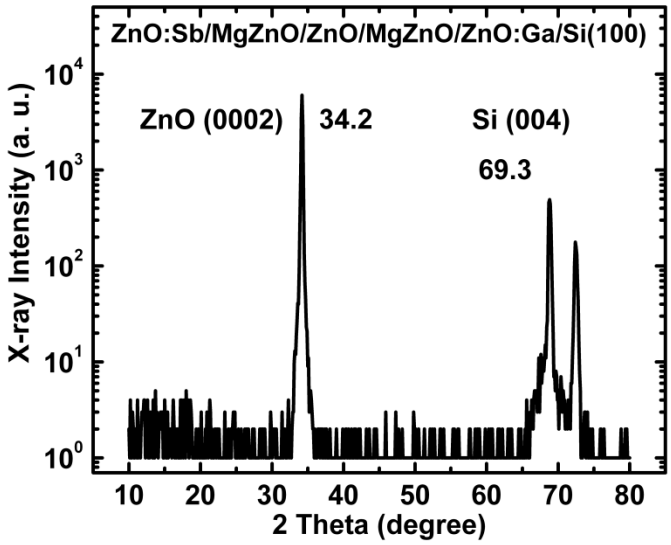

Figure 4.5 X-ray diffraction result of ZnO/MgZnO double heterojunction structure grown on Si (001) substrate

The elemental distribution of Zn, O, Mg, Sb, Ga and Si was obtained by performing SIMS measurements, as shown in Fig. 4.6 Dominant distribution of Sb and Ga dopants are in p-type and n-type layers, respectively. And Mg profile shows that the MgZnO/ZnO/MgZnO well is formed in between Ga-ZnO and Sb-ZnO layers.

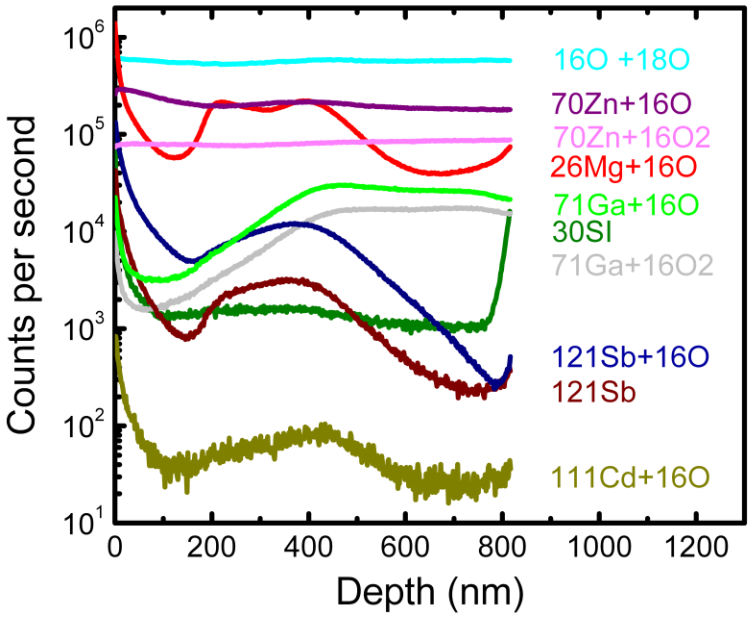

Figure 4.6 SIMS result of ZnO p-n junction on Si (100) substrate. The elemental profiles of Sb, Ga dopants, Zn, O, Mg and Si substrate can be seen.

I-V characteristics were measured using Agilent 4155C semiconductor parameter analyzer and Signatone probe station, as shown in Fig 4.7. The inset figure shows fairly good ohmic contact made by Au/Ti for n-layer and Au/Ni for p-layer. The diode shows fairly good rectification behavior with a threshold voltage of about 2.5 V, comparable to the threshold voltage of p-n homojunction diode. These results suggest that the thin MgZnO layers do not make difficulties to electrons and holes injecting to the well area.

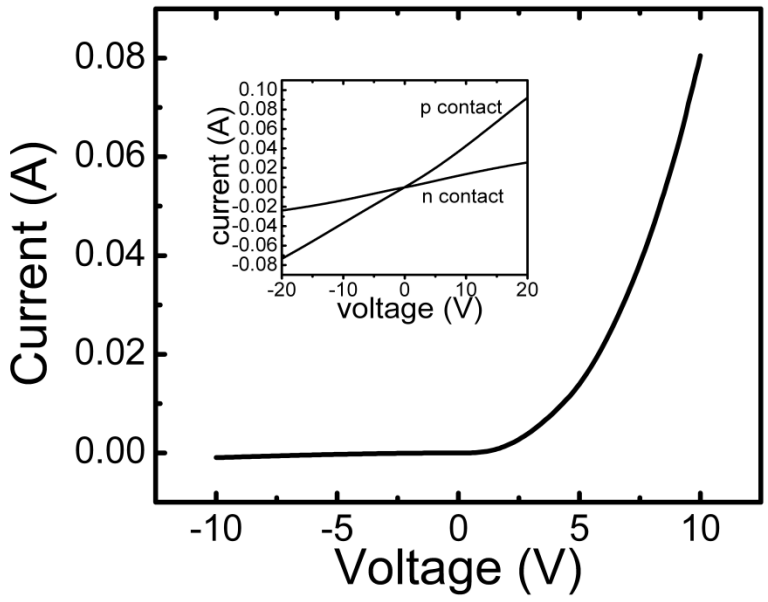

Figure 4.7 I-V characteristics of the p-n homojunction diode, showing typical rectifying characteristics. The inset shows the I-V curve of both n-type and p-type contacts.

EL measurements were performed using an Oriel monochromator and photomultiplier tube at room temperature. The diode was biased under DC forward voltages. Figure 4.8 shows the EL spectra obtained at different injection current. Near band edge emission at 3.2 eV appears when the current is 40 mA, while in ZnO homojunction device it starts to appear when the current is larger than 60 mA.[5] Afterwards, the intensity of this emission increases as the injection current increases from 40 mA to 80 mA. There is an abnormal decrease of intensity when the current increases from 50 mA to 60 mA and the intensity almost has no change as the current changes from 70 mA to 80 mA. This is due to the heat effect as a result of the increasing current through the diode, as well as current overflow effect in DH structure. Moreover, the near

band edge emissions also show redshifts with increasing current due to heat induced bandgap reconstruction.

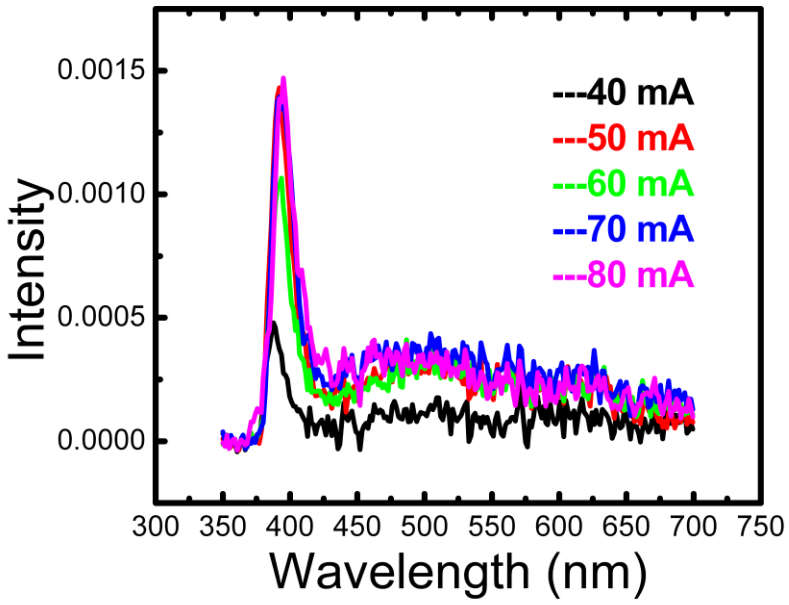

Figure 4.8 Electroluminescence spectra of double heterojunction ZnO diode at room temperature, with increasing injection current from 40 mA to 80 mA.

Figure 4.9 shows the comparison of EL emission spectrum between double heterojunction and homojunction devices under the same injection current of 70 mA. The homojunction consists of the same n-ZnO and p-ZnO layrs without the middle MgZnO/ZnO/MgZnO double heterostructure. The two devices were measured under same optical system at room temperature. Relative output power could be calculated by integrating intensity with step of energy. The calculated output power of heterostructure device is 7.3 times as p-n homojunction device. The improvement shall come from the

confinement effect of electrons and holes made by MgZnO barrier layers, since the other parameters of the device is designed to be the same as homojunction structure.

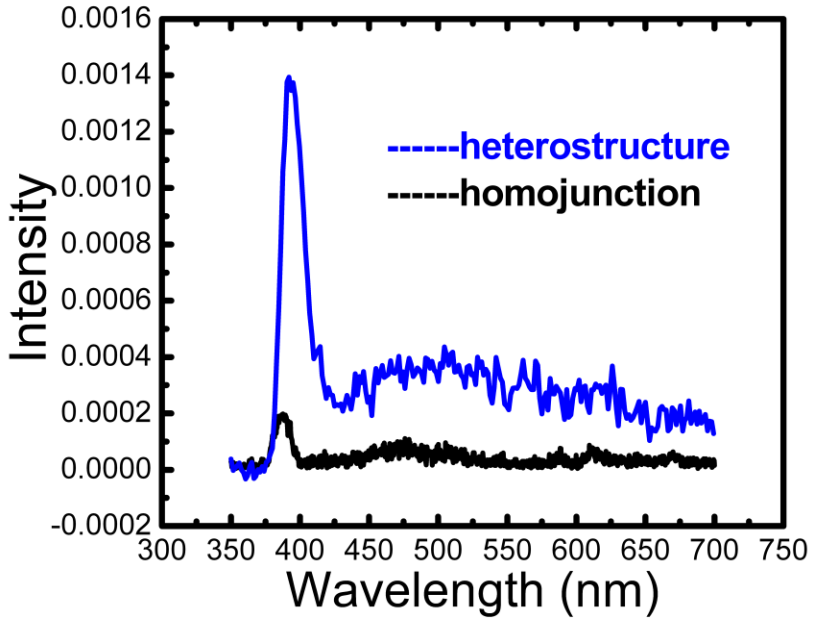

Figure 4.9 Electroluminescence spectra of double heterojunction ZnO diode and the p-n junction diode at room temperature, with 70 mA injection current.

4.4 Conclusion

In summary, UV MgZnO/ZnO/MgZnO double heterojunction light-emitting diode on Si (100) substrate has been realized. Au/Ni and Au/Ti make good Ohmic contacts to p-type and n-type ZnO layers. I-V measurement shows good rectification behavior and EL experiments demonstrate dominant UV emissions. Compared to ZnO homojunction diode, the output power of this device is 7.3 times stronger at the same injection current, which demonstrates a better confinement of electron and holes to recombine in an intrinsic ZnO layer.

4.5 References

[1] F. X. Xiu, Z. Yang, L. J. Mandalapu, D. T. Zhao, J. L. Liu, and W. P. Beyermann, Appl. Phys. Lett. 87, 152101 (2005)

[2] L. J. Mandalapu, F. X. Xiu, Z. Yang, and J. L. Liu, Appl. Phys. Lett. 88, 112108 (2006).

[3] L. J. Mandalapu, Z. Yang, F. X. Xiu, and J. L. Liu, Appl. Phys. Lett. 88, 092103 (2006).

[4] L. J. Mandalapu, F. X. Xiu, Z. Yang, and J. L. Liu, J. Appl. Phys. 102, 023106 (2006).

[5] J. Y. Kong, S. Chu, M. Olmedo, L. Li, Z. Yang and J. L. Liu, Appl. Phys. Lett. 93, 132113 (2008)

[6] F. K. Yam, Z. Hassan, Microelectronics Journal 36, 129 (2005)

[7] E. Fred Schubert, Light-Emitting Diodes, New York (2006)

[8] A. R. Brown, D. D. C. Bradley, J. H. Burroughes, R. H. Friend, N. C. Greenham, P. L. Burn, A. B. Holmes, and A. Kraft, Appl. Phys. Lett. 61, 2793 (1992)

[9] A. Zukauskas, M.S. Shur and R. Gaska, Introduction to Solid-State Lighting, Wiley, New York (2002)

[10] Frank M. Steranka, AlGaAs red light-emitting diodes, in: G.B. Stringfellow, M. G. Craford, (Eds.), Hight Brightness Light Emitting Diodes, in: R. K. Willardson, E. R. Weber, (Eds.) Semiconductors and Semimetals, vol. 48, Academic Press, New York, 1997, p.65.

[11] B. C. De Loach, B. W. Hakki, R. L. Hartman and L. A. D'Asaro, Proceedings of the IEEE, 61, 1042 (1973)

[12] Y. S. Chiu, M. H. Ya, W. S. Su, and Y. F. Chen, J. Appl. Phys. 92, 5810 (2002)

[13] Y. W. Heo, Y. W. Kwon, Y. Li, S. J. Pearton, and D. P. Norton, Appl. Phys. Lett. 84,3474 (2004)

[14] X. Zheng, X. M. Li, T. L. Chen, C. Y. Zhang, and W. D. Yu, Appl. Phys. Lett. 87, 092101 (2005)

[15] Jae-Hong Lim, Chang-Ku Kang, Kyoung-Kook Kim, Il-Kyu Park, Dae-Kue Hwang, and Seong-Ju Park, Advanced Materials, 18, 2720 (2006)

Chapter V Development of ZnO nanowire laser with distributed bragg reflectors

5.1 Motivation

Ultraviolet (UV) semiconductor diode lasers are widely used in information processing, data storage, and biology. However, their applications have been limited by large size and high cost. Semiconductor nanostructures are thereby attracting tremendous attention for the next-generation nano lasers and waveguides. ZnO with a direct wide band gap of around 3.30 eV, is low-cost in synthesis, which makes it one of the most promising candidates to realize UV lasing at room temperature. Random lasing was detected in ZnO nanopowders, [1-3] nanowires, [4-7] polycrystalline films [8-10] under optical excitation. Since the random emissions from disordered ZnO media are directionless, [11,12] random laser poses potential limitation for some applications. On the other hand, it is highly desirable to achieve Fabry-Perot lasing from ZnO nanowires because the naturally formed flat ends of nanowires avoid the difficulty of cleaving smooth facets in order to sustain lasing, leading to coherent beams with reliable modes and controllable output. A great deal of effort has already been seen in optically pumped ZnO Fabry-Perot lasing, [13-16] as well as large scale growth of vertically aligned nanowires which is a necessity for commercial application.[17,18] Recently, we have achieved electrically pumped Fabry-Perot lasing in vertically aligned ZnO nanowires grown with a ZnO seed layer on sapphire substrate.[7] The cavity loss is large due to small reflectivity at ZnO/sapphire and ZnO/air interfaces, leading to a relatively high threshold.

In order to reduce the threshold pumping density and enhance laser performance, DBR structure is widely adopted in the vertical cavity semiconductor laser diodes. Nevertheless, DBR has been only seen recently to be used in GaN nanowire lasers,[19] and it has not been attempted in ZnO nanowire lasers. This may originate from the difficulty of precise deposition of desirable multi-layer DBR on the ends of the nanowires. In this chapter, we address this problem by growing vertically aligned ZnO nanowires on SiO_2/SiN_X DBR films and carrying out optical pumping of these nanowires. With the presence of DBR, the threshold of nanowire lasing is reduced and enhanced cavity performance is achieved.

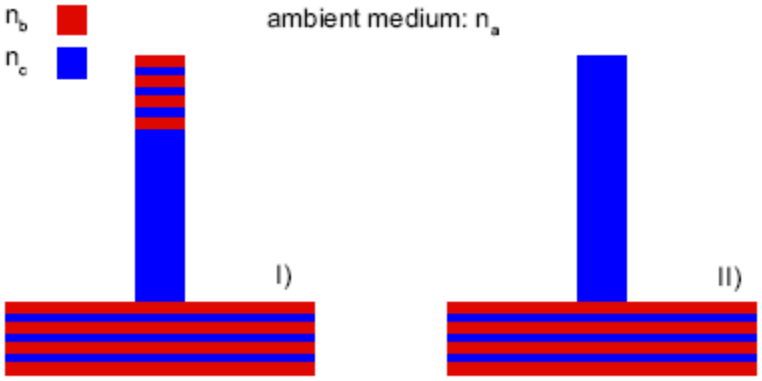

Figure 5.1 I) ideal cavity with DBR on both ends, II) practical design with DBR as substrate

5.2 Design and growth of DBR

For ZnO based laser devices, $Mg_xZn_{1-x}O$ with alternative x composition would be the ideal DBR material. However, it is hard to grow 2D film with controlled Mg incorporation rate. Here we develop other materials for the growth of high quality DBR structure. SiO_2 and SiN_x are the two materials we used in design of DBR structure. First,

the contrast of refractive index between SiO_2 and SiN_x is relatively large at working wavelength. The number of dielectric pairs required to achieve high reflectivity is therefore reduced.[20] Second, SiO_2 and SiN_x are insulators, which minimize the absorption at ZnO band edge energy. Third, both SiO_2 and SiN_x can be deposited by plasma-enhanced chemical vapor deposition (PECVD), and are a part of the standard process so low-cost production is possible.

SiO_2/SiN_X DBR structures were grown on c-plane sapphire substrates in plasma enhanced chemical vapor deposition (PECVD). Standard gaseous processes of SiO_2 and SiN_X were used. The plasma power was 25 watts at a source radio frequency of 13.56 MHz. The substrate temperature was 300 °C during the growth. The growth parameters were listed in Table 5.1

	SiH_4(sccm)	NH_3(sccm)	NO(sccm)	N_2(sccm)
SiO_2	200		400	900
SiN_x	200	4		500

Table 5.1 Growth parameters for SiO_2 and SiN_x by PECVD

5.3 Characterization of DBR -Method of transmission line

The most direct way to calculate the transmittance and reflectance of a DBR stack is to model it as a transmission line. The assumption is that the structure is homogeneous on the plane perpendicular to the direction of propagation, or k. If we pick the positive z axis as the direction of propagation, then $k=kz\times Z$, where $kz=2\pi n/\lambda$ is the propagation

constant, n is the refractive index and λ is the corresponding wavelength. In a one dimensional model, the 2×2 matrix, [M], relates the four field parameters in Fig.5.2. It includes the forward and backward propagating electric fields on the two sides of the layer. Only normal incident beam is considered in our assumption, since the experiment was performed at normal incidence.

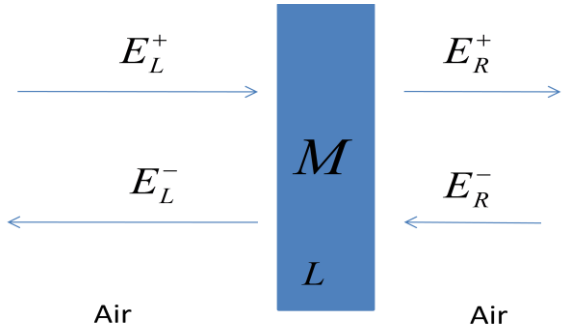

Figure 5.2 One layer model of transmission line method

In one layer case, as shown in Fig.5.2, the electric fields are described as

$$\begin{bmatrix} E_L^+ \\ E_L^- \end{bmatrix} = \begin{bmatrix} e^{-j\theta} & \\ & e^{i\theta} \end{bmatrix} \begin{bmatrix} E_R^+ \\ E_R^- \end{bmatrix}$$

$$= \frac{1}{2}\begin{bmatrix} 1 & -1 \\ 1 & 1 \end{bmatrix} \begin{bmatrix} \cos\theta & \frac{i\sin\theta}{n} \\ i n \sin\theta & \cos\theta \end{bmatrix} \begin{bmatrix} 1 & 1 \\ -1 & 1 \end{bmatrix} \begin{bmatrix} E_R^+ \\ E_R^- \end{bmatrix}$$

$$= [B_0]^{-1}[M][B_0] \begin{bmatrix} E_R^+ \\ E_R^- \end{bmatrix}$$

In which, $\theta = k_z L$, and L is the thickness of the media; $[B_0]$ represents the matrix induced by air, and is described as $[B_0]=\begin{bmatrix} 1 & 1 \\ -1 & 1 \end{bmatrix}$. If the layer is inserted in the media other than air, it describes as $\begin{bmatrix} 1 & 1 \\ -n & n \end{bmatrix}$, n is refractive index of the media. Similarly, if

considering multiple layers with a substrate, as shown in Fig. 5.3, the equation is then described as

$$\begin{bmatrix} E_L^+ \\ E_L^- \end{bmatrix} = [B_0]^{-1} \{[M_1][M_2]\}^N [B_{Sub}] \begin{bmatrix} E_R^+ \\ 0 \end{bmatrix}$$

where $M_{1,2} = \begin{bmatrix} \cos\theta_{1,2} & \frac{i\sin\theta_{1,2}}{n_{1,2}} \\ in_{1,2}\sin\theta_{1,2} & \cos\theta_{1,2} \end{bmatrix}$ represents the matrix element for the alternative layer.

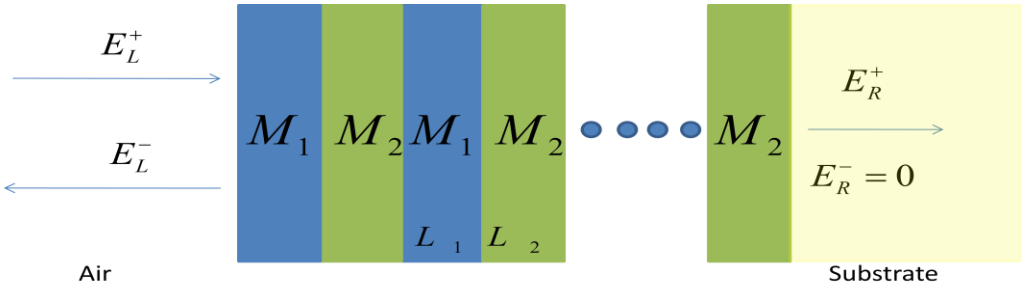

Figure 5.3 Multi layer model for transmission line method

Obviously, the resonant maximum occurs when the effective thickness of each layer is ¼ λ. The reflectivity r and transmissivity t can be described as

$$r = \frac{E_L^-}{E_L^+} = \frac{m_{21}^T}{m_{11}^T}$$

and $t = 1 + r = \frac{m_{11}^T + m_{21}^T}{m_{11}^T}$. The reflectance and transmittance are $R = |r|^2$, $T = |T|^2$ respectively.

5.4 DBR quality

The morphology of the DBR structures was characterized using SEM. The SEM image shown in Fig.5.4 is the cross section of the DBR layers on top of the sapphire substrate. As seen from the image, the interfaces between SiO_2 and SiN_x are fairly smooth, hence the interface scattering between the layers is minimized.

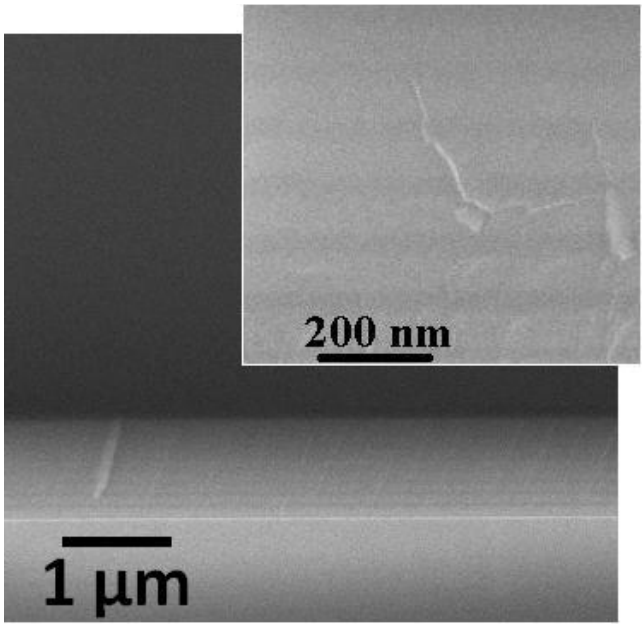

Figure 5.4 SEM cross section view of SiO_2/SiNx DBR grown on sapphire substrate

Reflectance of the DBR structures was measured using a Shumadzu UV-3101PC spectrometer. The reflectance spectrum was converted by a transmission measurement under normal incidence from 250 nm to 800 nm, with the assumption that the absorption in the measurement is zero.[21,22] Total 10 pairs of SiO_2 and SiN_X layers of 60.9 nm and 48.7 nm, respectively, are observed. The thicknesses match with $\lambda/4$ requirement of SiO_2 and SiN_x layers, with a consideration of the refractive index of 1.56, and 1.95, respectively. Fig. 5.5 shows the transmission spectrum of the DBR with the simulation

result plotted as well. It is clear that there is an intensive UV absorption of this structure below 400 nm.

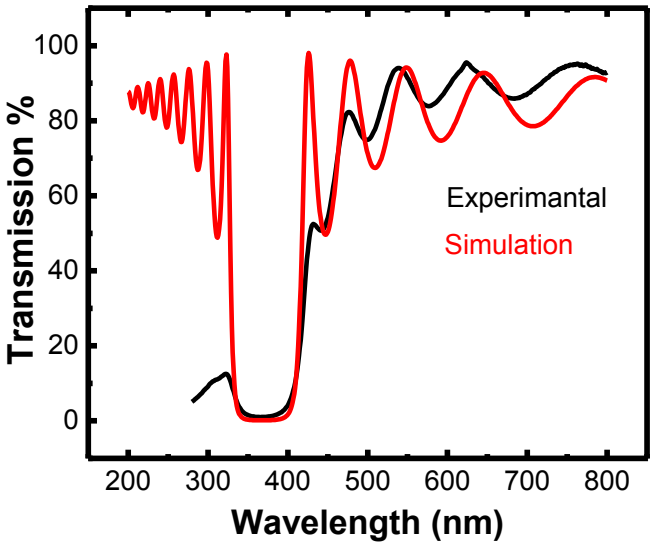

Figure 5.5 Transmission spectrum of the DBR grown on sapphire substrate, with simulation result plotted in red.

The absorption is proven to be from SiNx layer as compared between SiO_2 and SiN_x single layer absorption spectrum in Fig.5.6. The UV absorption from SiN_x is possibly due to the N vacancy.[23] To diminish the UV absorption in SiNx, N/Si ratio needs to be tuned during growth.[24] According to ref. 24, absorption edge blueshifts as increased N/Si ratio.

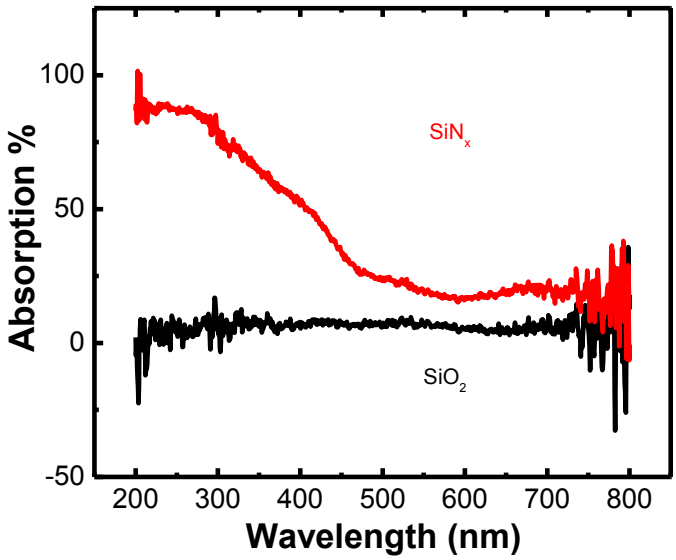

Figure 5.6 Absorption of single layer SiO_2 and SiN_x materials grown on sapphire substrate by PECVD

Figure 5.7 shows the transmission spectrum from four sample grown under different NH_3 flow rate. It is clear that when the NH_3 flow rate is up to 16 sccm, there is no UV absorption above 360 nm.

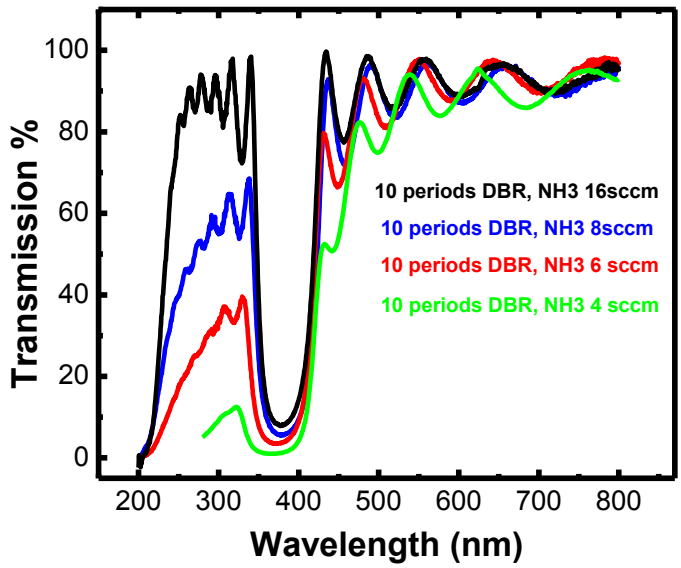

Figure 5.7 Transmission spectra from 10 periods DBR structures grown under different NH_3 flow rates.

Figure 5.8 shows reflection spectra of this DBR structure from the measurement and simulation based on transfer matrix method, with an assumption that there is no absorption occurred. It is evident that both calculated and measured results are in good agreement, indicating that the DBR gives desirable optical quality and the reflectivity at 380 nm-390 nm reaches 95%.

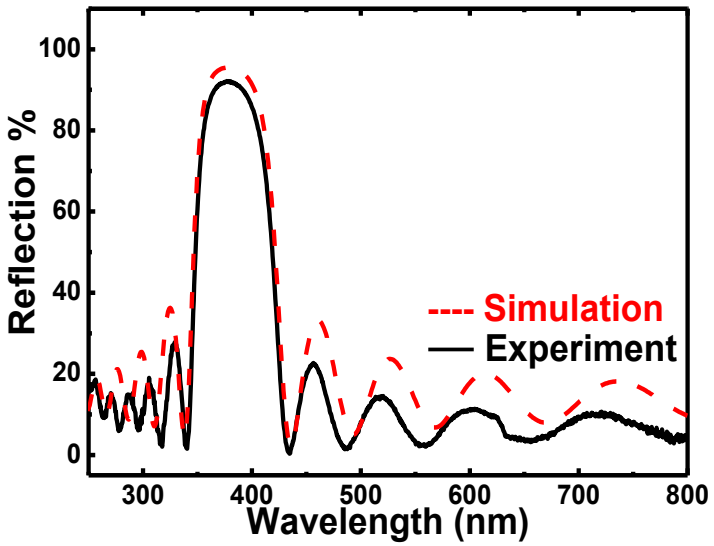

Figure 5.8 Measured and simulated reflectance of 10 periods DBR structure grown with 16 sccm NH_3 rate.

5.5 Growth of ZnO nanowires

After the DBR was fabricated, the sample was transferred to a MBE system. The MBE process started with a few nanometers of ZnO buffer layer growth at 350 °C, and followed by one micron ZnO layer growth at 550 °C. The polycrystalline ZnO thin film consists of closely packed column structure. The c-axis of ZnO grain is highly directional, which is perpendicular to the substrate plane. This polycrystalline layer acts

as seed layer for the subsequent vertically aligned ZnO nanowire growth. The morphology of the seed layer is important for the growth of vertically aligned nanowires. The growth mechanism is described as follows. As the reaction temperature is above the melting point (419 °C) but lower than the boiling point (907 °C) of Zn or ZnO, a liquid phase Zn/ZnO should first form at an early stage on the buffer layer. The liquid droplets solidify quickly by oxidation and nucleate in to nanoparticles.[25] The metallic Zn source in the boat, which is highly reactive, is subjected to oxidation and covered by oxide coatings. These oxide coatings will hinder the evaporation of Zn and thus decrease the Zn/ZnO vapor pressure. Such gradual diminishing source vapor will lead to formation of small-sized structures, which was observed by Wu et.[26,27] Nucleation of Zn/ZnO atoms will be preferred at thermodynamically active sites. These sites would be the tips of the ZnO convex seed layer, which have lower surface energy compared to the other surface area. Thus the direction of nanowire growth is strongly related to the surface morphology of the seed layer. Figure 5.9 shows the early stage of growth process, it is clear that the nanowires tend to grow at the tips of the buffer surface.

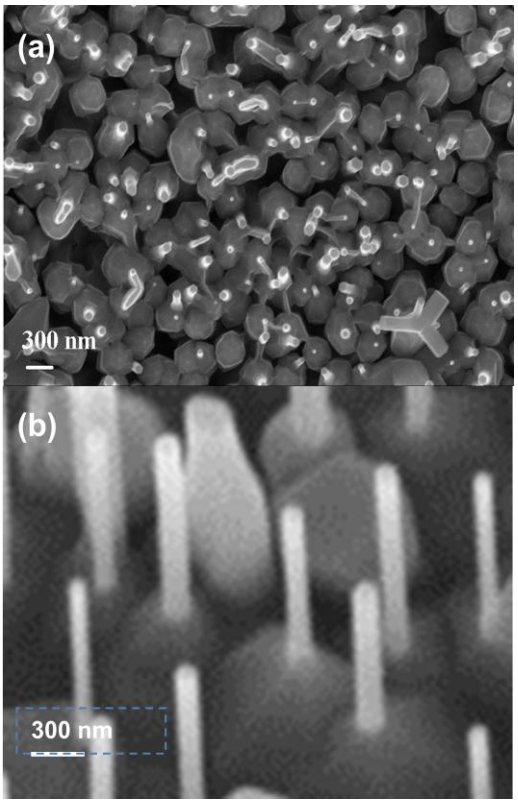

Figure 5.9 Early stage of nanowire growth on polycrystalline buffer layer

Under this consideration, the surface morphology is optimized to favor the vertical growth. Figure 5.10 shows the surface morphology of ZnO seed layer grown on the DBR structure with different growth time varying from 60 minutes to 150 minutes. The convex pyramids were formed when the seed layer is as thick as 1 μm with growth time 150 minutes.

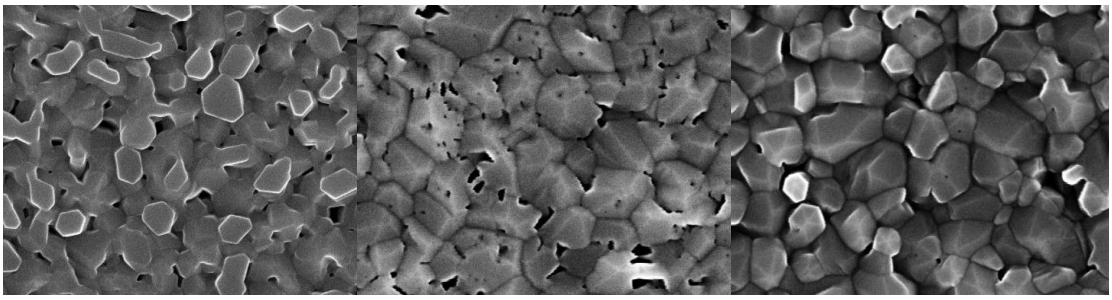

Figure 5.10 SEM top view of ZnO polycrystalline buffer layer grown on DBR, with different growth time (a) 60 mins, (b) 120 mins, (c) 150 mins

ZnO nanowires were then grown on top of the column structured ZnO layer by chemical vapor deposition (CVD). The CVD is a horizontal quartz tube furnace system (Thermal Scientific Inc.). Zinc powder (99.999% sigma Aldrich) in a glass bottle was placed in the center of the tube, with the ZnO sample placed about 8 cm downstream from it. A flow of 606 sccm of nitrogen was passed continuously through the furnace. The source and sample were then heated to 515 °C at a ramp rate of 30 °C per minute. Once the temperature was reached, 188 sccm flow of a mixture of argon/oxygen (99.5:0.5% by volume) was introduced to the tube for ZnO nanowire growth for 15 minutes, named sample #1.

5.6 Characterization of nanowires

Nanowires were characterized using SEM and TEM. Regular photoluminescence spectrum was acquired from the excitation by a 325 nm He-Cd laser. Figure 5.11 shows the characterization results from the nanowires grown on 1 μm ZnO polycrystalline buffer layer. Figure 5.11 (a) and (b) show top-view and side-view SEM images of the nanowire sample, respectively. The as grown ZnO nanowires follow the c-axis of the ZnO grains of the seed film, and are vertically aligned. The lengths of nanowires range

from 10μm to 11μm, while the diameters of nanowires range from 50 nm to 300 nm. Figure 5.11 (c) shows a TEM image of a typical single nanowire, revealing a single-crystal wurtzite structure. A selected area electron diffraction pattern confirms that the nanowire grows along c-axis, as shown in the inset of Fig. 5.11 (c). Figure 5.11 (d) shows a PL spectrum of the nanowires measured at 10K. There are three peaks, which are related to donor-bound exciton (D_0X), donor-acceptor pair recombination and its phonon replica, indicating good optical quality.

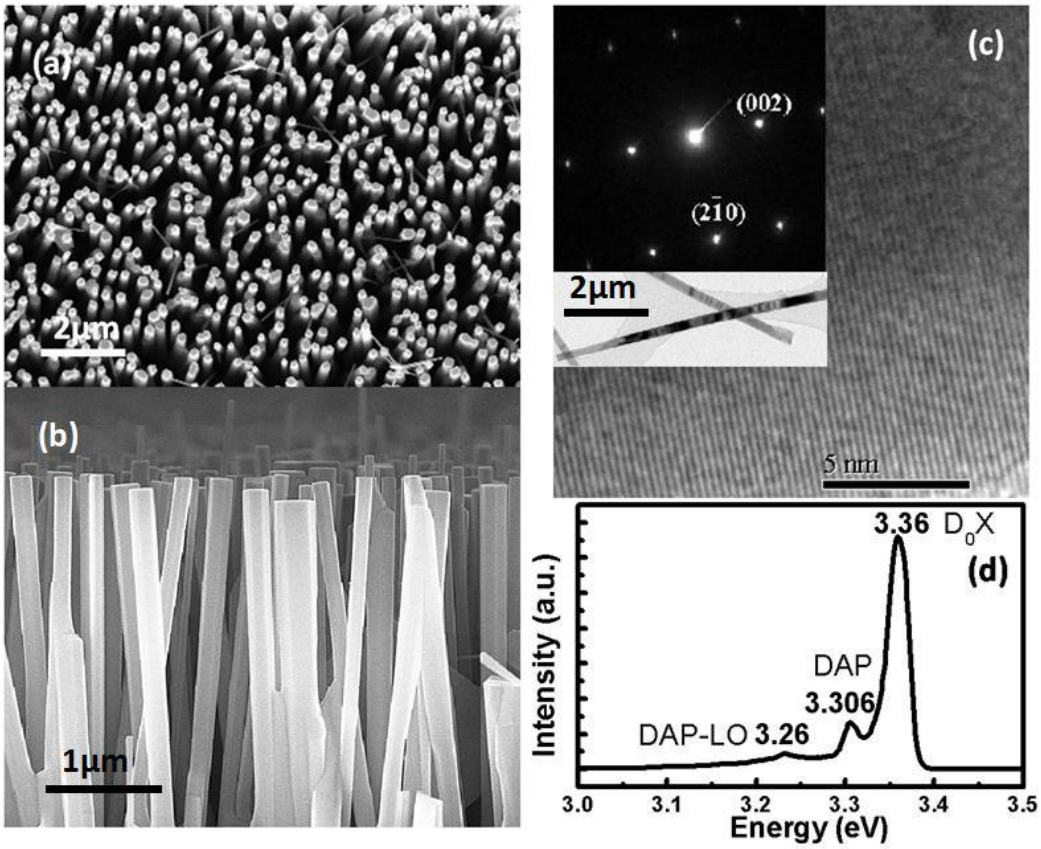

Figure 5.11 Top view SEM image of the vertically aligned nanowires grown with a ZnO seed layer on DBR structure. (b) Side view SEM image of the vertically aligned nanowires. (c) High-resolution TEM image of one nanowire. Inset shows a lower magnification TEM image of nanowires and corresponding electron diffraction pattern. (d) PL spectrum of the sample excited by 325 nm excitation laser at 10 K.

High-intensity optical pumping was carried out using the frequency-tripled output (355 nm) of a Nd:YAG pulse laser with a repetition rate of 10 Hz and 3 ns pulse duration. The excitation laser beam was focused to form an excitation spot of 14 μm in diameter on the nanowires. A charge coupled device (CCD camera) with a choice of high resolution was used to detect the emission, which was coupled into an optical fiber. The data was collected using a computer.

Figure 5.12 shows the evolution of the luminescence spectra at the excitation intensity ranging from 45 kW/cm^2 to 500 kW/cm^2. At low excitation power, a broad emission with peak energy at 3.23 eV is evident, which corresponds to ZnO near band edge spontaneous emission. As the excitation power increases, several sharp peaks with full width at half maximum (FWHM) of about 3 meV start to shoot up, indicating an onset of lasing emission. For comparison, the emission of the same length nanowires without a bottom DBR structure with different pumping power from 45 kW/cm^2 to 500 kW/cm^2 is shown in the inset of Fig. 5.12. Note that the lasing modes are distributed on a broad spontaneous emission, which is from the body emission of the non-lasing nanowires. [28] As seen in Fig. 5.11 (a) and (b), the nanowires have size variation, it is possible that only a few nanowires within excited area lase, while the others remain spontaneous emissions. Although is shows one dominant peak in the PL spectrum, the reference nano laser without DBR structure is not a single mode laser because with increased input pumping power, more modes arise. There is no suppression effect for weaker modes as the intensity of all modes increases with the increase of pumping power. It is typical for nanowire lasers. Ref. 4, Ref. 7 and Ref. 28 reported that their

samples exhibited the same phenomenon as our sample. In Ref. 4, single lasing mode was detected right above threshold, and more modes were observed with the pumping power much higher than the threshold.

To our best knowledge, the detected emission is a sum of emissions from multiple nanowires within the excitation beam, and each nanowire is a single cavity. In most cases, not all nanowires participate in lasing, some may only have spontaneous emission, some have multiple modes emissions and only few has single stimulated emission. Considering that there is no 'mode selection' technique performed in our experiment to select a single mode, it is reasonable to observe multiple modes output as described.

For our reference nanowire sample without DBR structure, the one mode at 388 nm is relatively strong compared to other modes, which may be due to a strong single mode emission from a single nanowire. However, this single mode does not dominate further at higher pumping power. So we do not consider a single mode lasing from the reference nanowire sample without DBR structure.

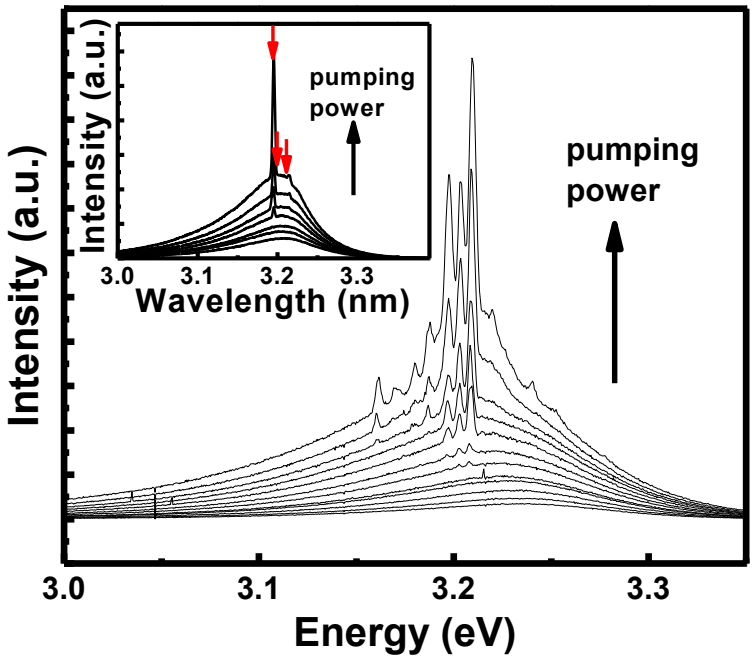

Figure 5.12 PL spectra of the vertically aligned nanowires with optical pumping power from 45 kW/cm^2 to 500 kW/cm^2. The inset shows the optically pumped PL spectra from a reference ZnO nanowire sample with the same length and no DBR underneath.

Due to strong spontaneous emission, the onset of lasing is difficult to observe from excitation power dependant intensity evolution. To separate the spontaneous and stimulated emissions, Gaussian fitting was carried out for the spectra of all excitation powers. Figure 5.13 shows the fitted result of the emission at 450 kW/cm^2, which is divided into 10 peaks consisting of two broad emission peaks and eight sharp peaks with even spacing.

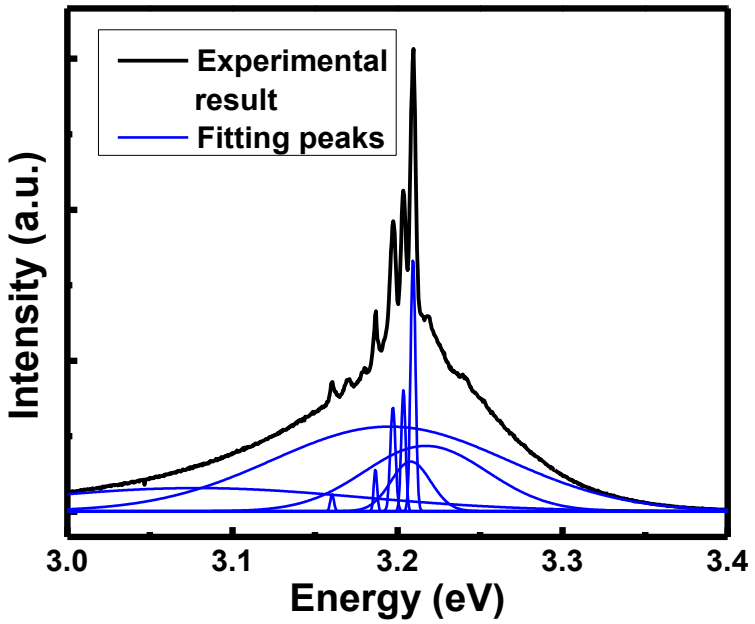

Figure 5.13 Emission of ZnO nanowires on DBR structure at pumping power of 450 kW/cm^2. The spectrum is fitted with multiple Gaussian peaks.

Figure 5.14 (a) and (b) show the integrated intensity vs. excitation power for the reference nanowire sample without DBR structure and the nanowire sample with DBR structure, respectively. The spontaneous emissions follow a sublinear evolution and the stimulated emissions show superlinear characteristic with clear onset lasing threshold. The power-dependent intensity can be well described by power law $y=ax^p$, with p=3.03 for reference nanowires and p=3.08 for nanowires grown on DBR. The two solid straight lines are drawn to guide eyes, indicating the threshold power of 121 kW/cm^2 and 150 kW/cm^2 for the samples with and without DBR, respectively. The 20% reduction of threshold can be explained by considering the threshold in a Fabry-Perot resonator, which is written as $g_{th}=\gamma+\frac{1}{2L}\ln(\frac{1}{R_1\times R_2})$,[29] where γ is the transition loss, L is the length of the nanowire, and R_1, R_2 denote the reflectivity at each end of the cavity. With the DBR

structure as the bottom reflector, the reflectivity increases from 3% (ZnO/sapphire interface) to 95%, leading to a lower threshold pumping power.

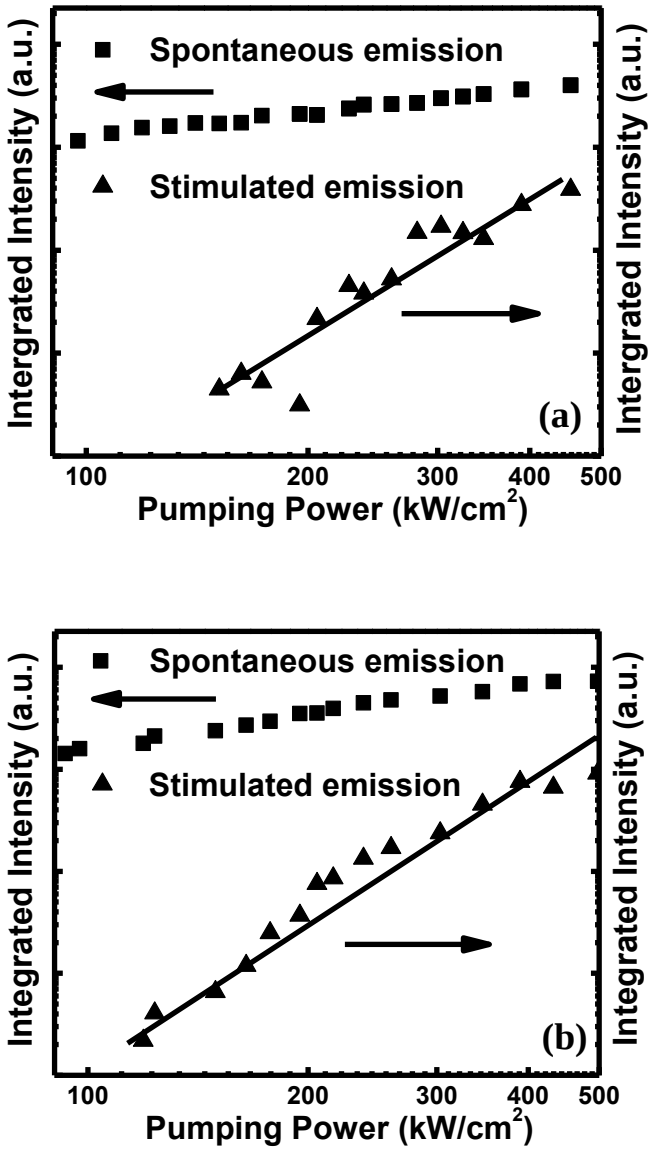

Figure 5.14 (a) Integrated intensity of spontaneous and stimulated emissions under different pumping power from the sample grown without DBR. (b) Integrated intensity of spontaneous and stimulated emissions under different pumping power from the sample grown on DBR structure.

The slope efficiency and saturation mechanism in our samples is discussed below. Similar to the results published in Ref. 28, near threshold, the Power(out)-Power(in) curve is super linear, which follows Power Law, and the simulation results in Fig. 5.15 showed a slightly larger power factor of 3.08 for the nanowires with DBR structures, compared to 3.03 for the reference nanowires. The super linear relation in Power(out)-Power(in) curve indicates that excitonic recombination instead of electron-hole plasma (EHP) recombination plays the dominant role in the gain generation at this pumping level (see Ref. 28 and pre-print 'Room temperature one-dimensional polariton condensate in a ZnO microwire' at arXiv.org > cond-mat > arXiv: 1007.4686). The larger exponential coefficient indicates higher 'slope' efficiency in the log-scale plot.

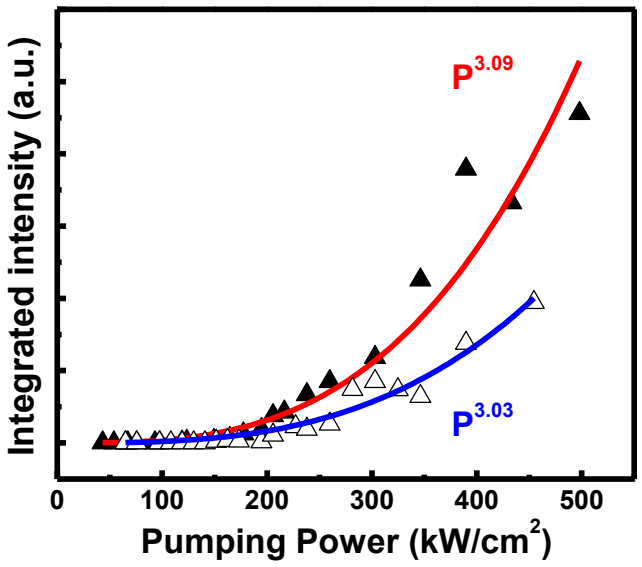

Figure 5.15 Integrated intensity of lasing from reference nanowires and nanowires grown with a DBR structure

Figure 5.16 (a) shows lasing spectrum at the pumping power of 500 kW/cm^2 in comparison with the calculated Fabry-Perot cavity modes confined in a Gaussian distributed peak with center energy at 3.20 eV. The mode distribution was obtained by using Airy function $A=[1+F\sin^2(\omega/2)]^{-1}$, where ω is circular frequency, which can be transformed from energy, and F is cavity finesse, which can be written as $F=\frac{4(R_1R_2)^{1/2}}{[1-(R_1R_2)^{1/2}]^2}$. For the nanowires grown on DBR structure R_1=95%, R_2=18%, F is calculated to be 4.8, which is greatly enhanced from 0.34 for the nanowires grown without DBR on sapphire substrate. Considering that the average length of the nanowires is 10 um, and the refractive index of ZnO at band edge follows the expression $n'=n-\lambda(dn/d\lambda)$, where n=2.5 is the refractive index of ZnO below band edge and $dn/d\lambda$=-0.015 nm^{-1} denotes the dispersion relation for the refractive index,[30] the simulated mode distribution is in close agreement with the observed experimental result, i.e., evenly distributed mode spacing of about 1nm (6meV). The peak positions and mode spacing stay the same under different excitations as well, which is a strong evidence of Fabry-Perot type resonance. [31]

Figure 5.16 (b) shows the statistic distribution of experimental quality factor (Q) as a function of pumping power above thresholds for the two samples with and without DBR structure, respectively. The dashed lines denote average *Q* factors for the two samples. The *Q* factor increases from 865 for the sample without DBR to 1067 for the sample with DBR, indicating higher performance of the cavity thanks to the larger reflectivity from DBR. With increased excitation power, the Q factors appear to decrease owing to the heat induced FWHM expansion.

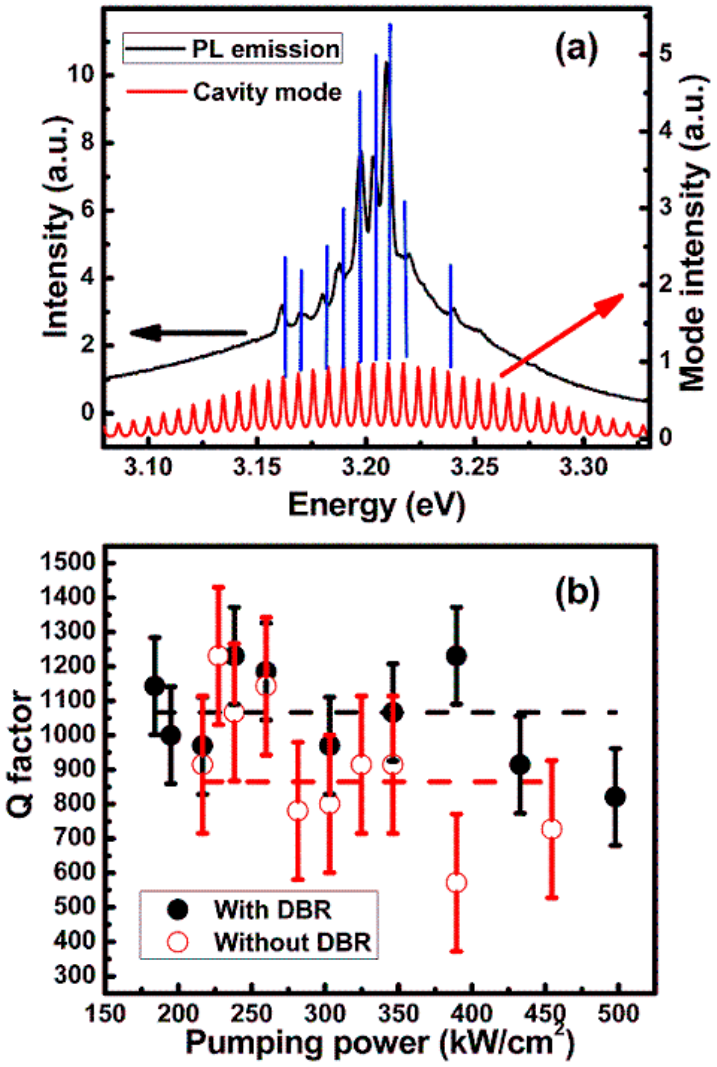

Figure 5.16 (a) PL spectrum at excitation power of 500 kW/cm^2, with the calculated mode distribution at different energy. (b) Quality factor *Q* distribution from the two nanowire laser samples with and without DBR structure

Figure 5.17 shows lasing spectra at higher excitation power between 500 and 1870 kW/cm^2. Stronger lasing modes superimposing on the broad near band edge spontaneous

emission peak are evident. The right top inset is Gaussian fitted result of the emission with excitation power at 1870 kW/cm^2.

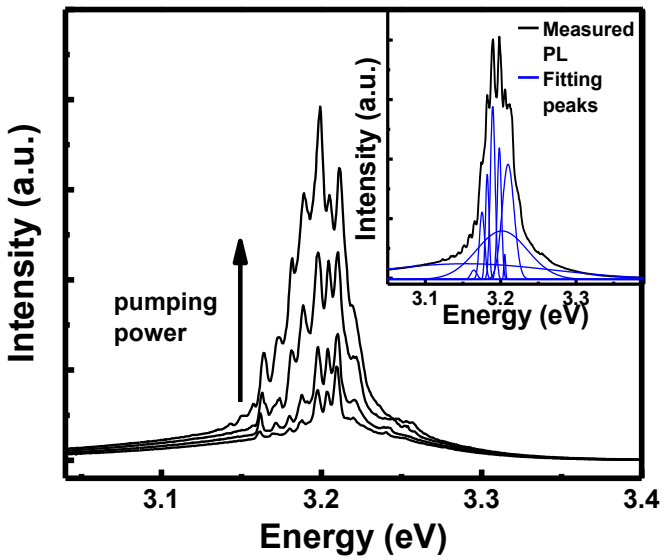

Figure 5.17 PL spectra of the vertically aligned nanowire laser sample with DBR at the pumping power from 500 kW/cm^2 to 1870 kW/cm^2. The top right inset shows a typical emission at 1870 kW/cm^2, with multiple peaks fitted by Gaussian distribution.

When the pumping power goes up to 500 kW/cm^2, the super linear characteristic evolves into linear characteristic, which indicates the transition of excitonic process into EHP process, as shown in Fig.5.18. The linear fitting in high pumping power region shows that the slope efficiency of DBR sample is higher than that of reference sample, which is consistent with the results observed in the super linear part. Since ZnO has the natural advantage of realizing low threshold laser, the low power part with excitonic emission is attractive. The slope efficiency is already discussed in the low power region, and the purpose of our experiment is to achieve lower threshold, so the higher pumping power region is not discussed here.

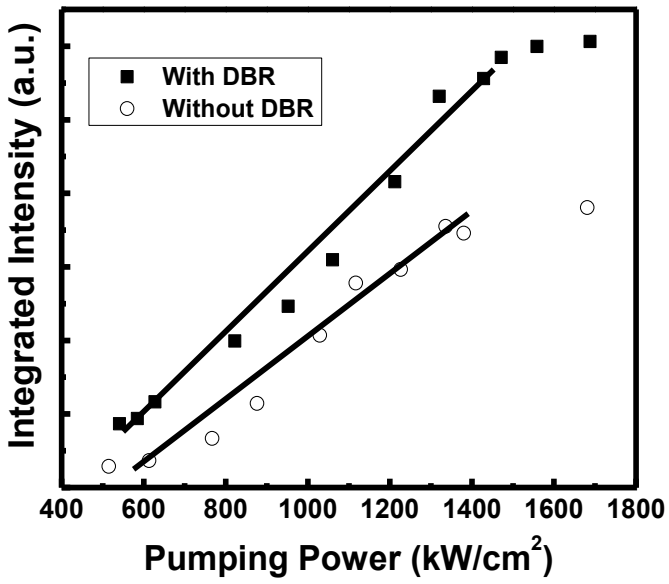

Figure 5.18 Integrated intensity of lasing from reference nanowires and nanowires grown on DBR structure at high pumping power

The saturation levels of the two samples are very close. There are two reasons. First, simple gain saturation analysis using $g = g_0 \exp[L/Ls]$ does not explain the phenomenon observed in our experiments because the calculated saturation power is orders of magnitude higher than our experimental results. Considering the transient thermal population and the participation of non-radiative recombination, the power saturation level is mainly determined by the material properties. The influence from cavity improvement is very limited.

The intensity ratio between stimulated emission and spontaneous emission increases with the increase of excitation power (shown in Fig. 5.19), which means that the stimulated emission intensity grows faster than spontaneous emission. The lasing modes at high excitation range are also stable, though there is a slight blueshift, compared

with those at excitation power less than 500 kW/cm^2. The blueshift is mainly due to temperature induced refractive index variation.[32]

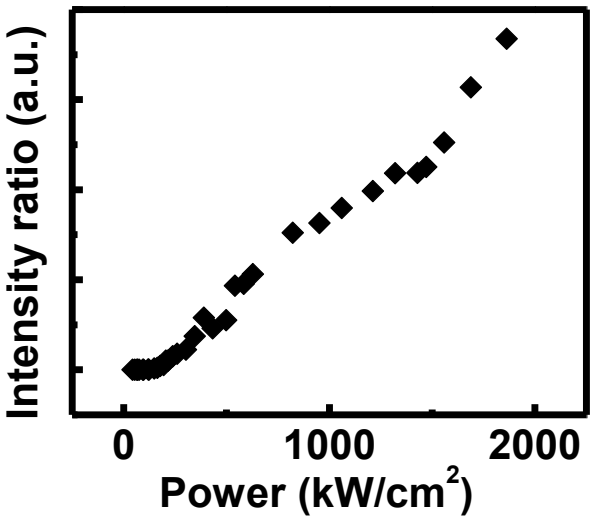

Figure 5.19 Integrated intensity ratio between stimulated emission and spontaneous emission above threshold.

5.7 Nanowire length dependence

In order to further examine the relation between the cavity and its lasing action, optical pumping PL experiments were performed on ZnO nanowires with different lengths grown on DBR structure. Sample #2 and Sample #3 were grown on the same ZnO buffer on DBR structure as Sample #1. The growth time were controlled to lead to shorter nanowire lengths. The growth parameters were listed in Table 5.2

	O_2/Ar (sccm)	N_2 (sccm)	Temperature (°C)	Growth time (min)
Sample #1	188	606	515	15
Sample #2	188	606	515	12
Sample #3	188	606	515	8

Table 5.2 Growth parameters of nanowires on DBR structure

Figure 5.20 shows SEM images from Sample #2 and Sample #3, showing that both samples have vertically aligned nanowire growth. The nanowire lengths were 4 μm and 1 μm respectively. The nanowire growth does not follow the linear trend.

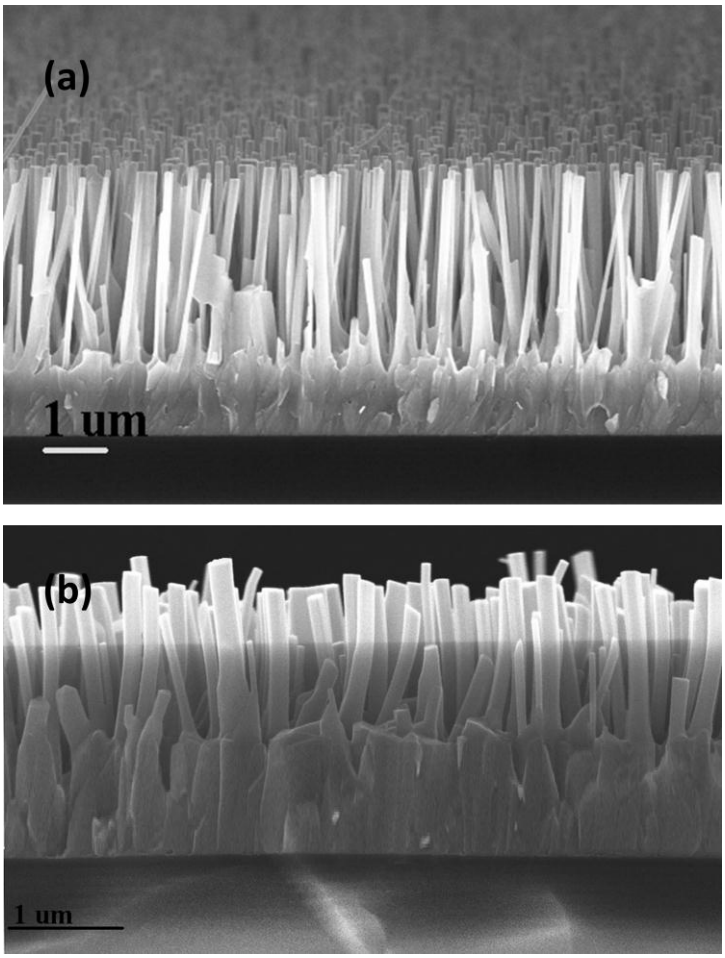

Figure 5.20 SEM cross section view of nanowires for Sample #2 and Sample #3

Figure 5.21 shows the PL emission from sample #2, with excitation power from 150 kW/cm^2 to 2000 kW/cm^2. ZnO near band edge spontaneous emission was observed at low excitation power. As the excitation power increases, several sharp peaks with full width at half maximum (FWHM) of about 4 meV start to shoot up, indicating an onset of lasing emission.

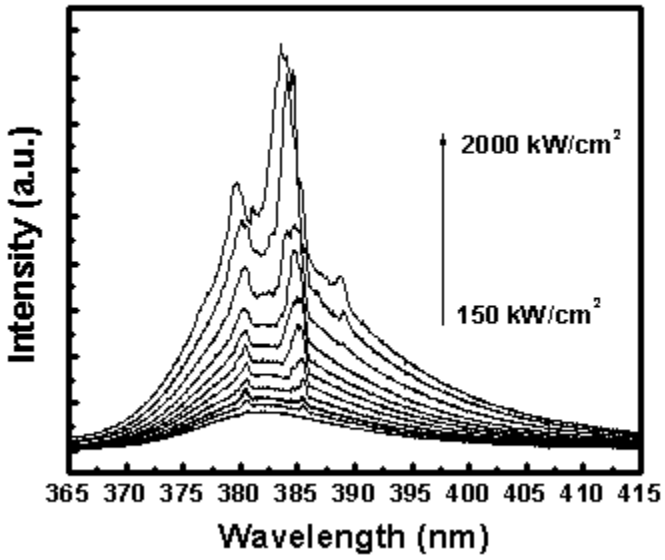

Figure 5.21 PL spectra of the vertically aligned nanowires with optical pumping power from 150 kW/cm^2 to 2000 kW/cm^2.

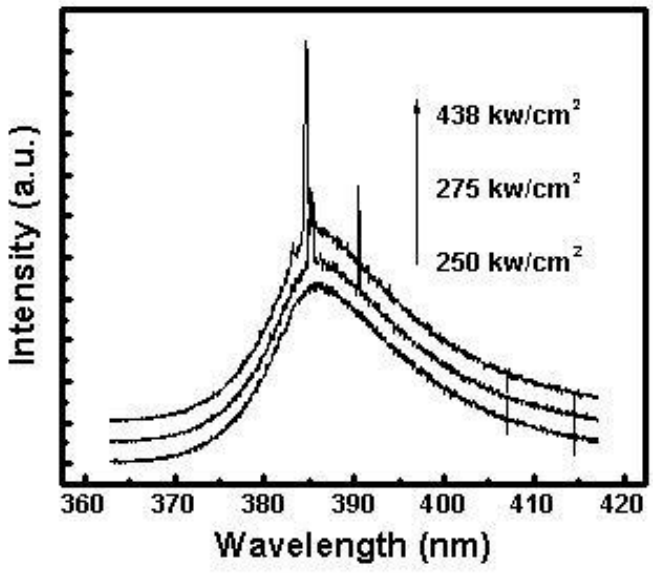

Figure 5.22 PL spectra of the vertically aligned nanowires with optical pumping power from 250 kW/cm^2 to 438 kW/cm^2.

Figure 5.22 shows the PL emission from sample #3, with excitation power from 250 kW/cm^2 to 438 kW/cm^2. The threshold pumping power for each sample was measured as 200 kW/cm^2 and 275 kW/cm^2 respectively.

For sample #2, gaussian fitting was performed to separate the peaks, as shown in Fig. 5.23. The emission consists of spontaneous and stimulated emissions. Two stimulated emission peaks were extracted from two broad spontaneous emission peaks. Figure 5.24 shows the integrated intensity of stimulated emission with different pumping power. The relation is super linear. It is clear that the evolution follows power law as we discussed before.

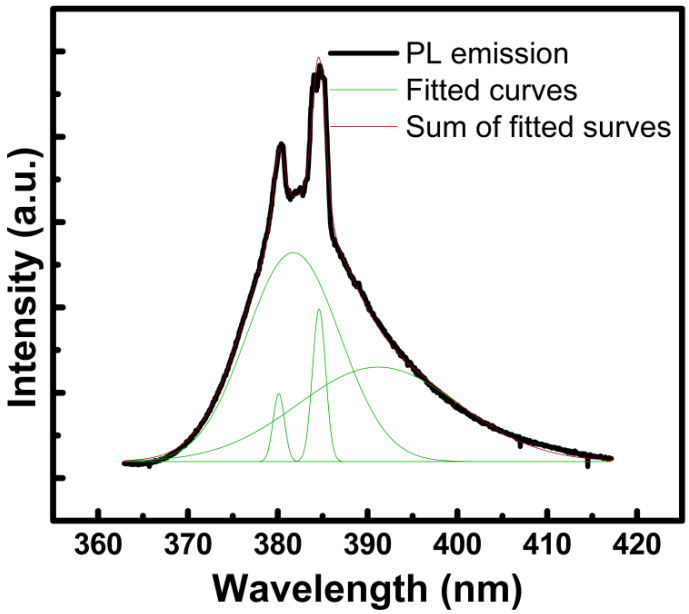

Figure 5.23 Emission of ZnO nanowires on DBR structure at pumping power of 926 kW/cm^2. The spectrum is fitted with multiple Gaussian peaks

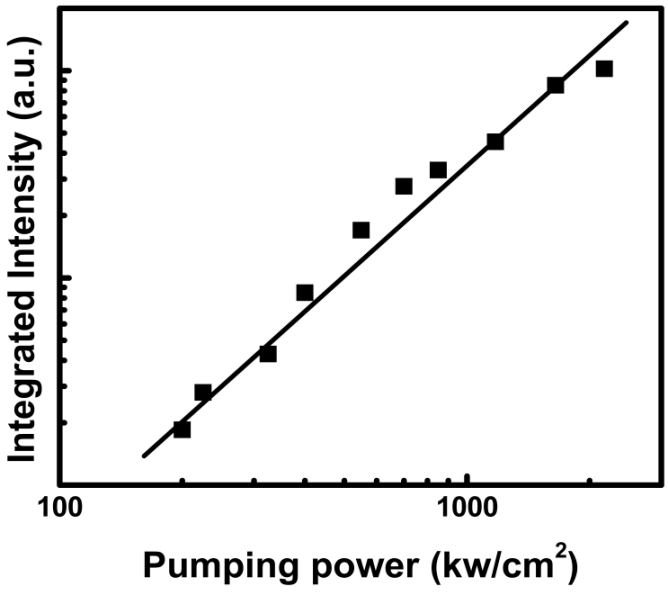

Figure 5.24 Integrated intensity of stimulated emissions under different pumping power from Sample #2 grown on DBR

For all the three samples with different lengths, the threshold pumping power and the lasing mode space are summarized in Fig 5.25. Equation $g_{th}=\gamma+\frac{1}{2L}\ln(\frac{1}{R_1\times R_2})$ was used to calculate the threshold power, which is strongly related to γ, L and R. Noted that when the nanowire length is 10 um, γ is the bigger weight for determining threshold power. The threshold drop of 20% for 10 um nanowires is thus a reasonable result, and it is due to the enhancement of reflectivity by DBR structures.

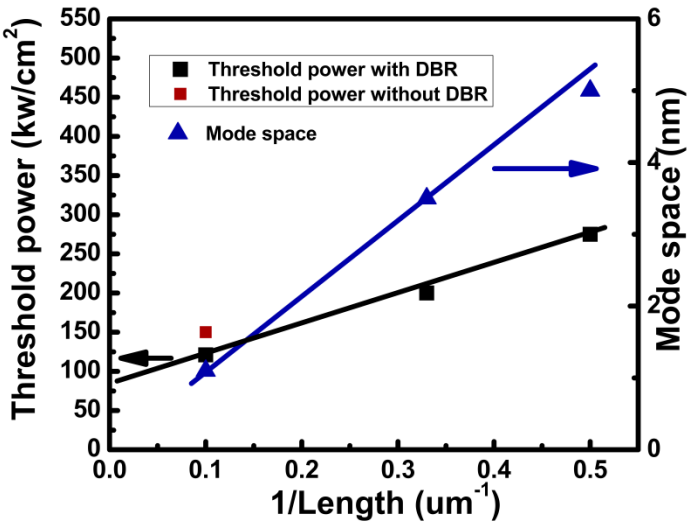

Figure 5.25 Threshold power and mode space for different length nanowires

5.8 Nanowire size limitation

The two broad peaks are spontaneous emissions, indicating that even at these very large pumping powers, there is coexistence of spontaneous and stimulated emissions.[33] Moreover, the intensity of the spontaneous emissions do not show saturation as the increase of the pumping power. This is mainly due to the statistical results of lasing from multiple nanowires with different sizes. Note that the excitation laser beam size is about

14 μm in diameter, the excitation area would contain hundreds of nanowires with size variation from 50 nm to 300 nm in diameter. The emissions from these nanowires have different modes reliability. Optical confinement becomes reduced due to the influence of diffraction effects. The effects can be qualitatively understood by considering the integrated internal and external electromagnetic field intensities for the cylindrical waveguide modes. A rough calculation of the fractional mode power within the core of the waveguide of radius r is given by

$$\eta = 1 - (2.405 \exp[-\frac{1}{V}]^2)V^{-3}$$

where $V=kr(n^2-1)^{1/2}$ and $k=2\pi/\lambda$.

A rough calculation shows that the fractional mode power within the core of the waveguide of 200 nm in diameter is about 90%. However, less than 25% of the field intensity is present inside the wire with diameter less than 100 nm.[34] Consequently, highly efficient confinement of light only occurs in the nanowires with diameters of 200 nm or larger. For the nanowires with small diameters, body emission will be dominant instead of resonant formation, leaving a broad emission peak even with very high pumping power above threshold.

The waveguide modes of the wires can be simulated with classical optical waveguide theory by the simulation software MODE Solutions. The results are shown in Fig. 5.26 for different size from 40 nm to 400 nm in diameter. It is consistent with the calculation above, showing that nanowires with size larger than 200 nm are able to hold the waveguide inside.

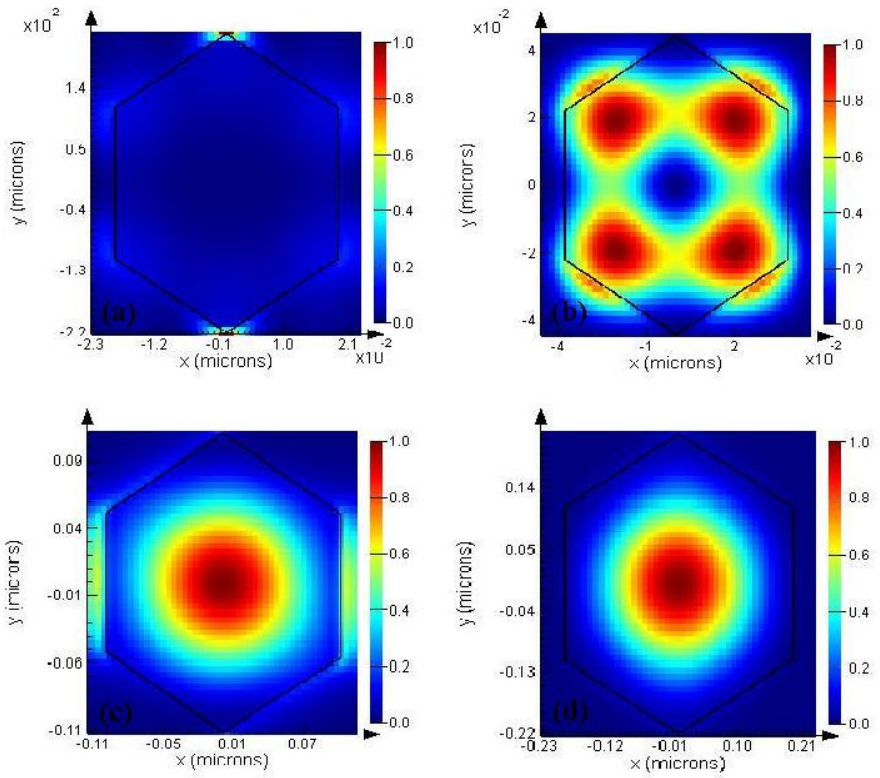

Figure 5.26 Electromagnetic field in nanowires with different in-plane sizes

5.9 Conclusion

In summary, we grew a 10-period DBR structure with designed thicknesses of the alternative layers made from SiO_2 and SiN_x. The reflectivity at 380 nm-390 nm reaches 95%. Vertically aligned ZnO nanowires were achieved by CVD growth, on a ZnO polycrystalline seed layer deposited on DBR by MBE. Fabry-Perot type lasing was observed with optical pumping and a lower threshold excitation power was achieved due to the lower cavity loss with the DBR structure. The cavity finesses is improved from 0.34 to 4.8 with one end DBR structure, hence the FWHM of lasing mode is reduced from 4 meV to 3 meV. The competition between spontaneous and stimulated emission was further studied at higher pumping power. The non-extinct spontaneous emission is

due to fractional confinement of waveguide modes in small nanowires less than 100 nm in diameter. The DBR technology can be transferred to Si or even glass substrate, further lowers the cost. The achievement of lower threshold pumping power with DBR structure paves a way for further development of low-threshold ZnO nanowire laser diodes.

5.10 References

[1] T. Nakamura, B. P. Tiwari, and S. Adachi, Appl. Phys. Lett. 99, 231105 (2011)

[2] H. Cao, J. Y. Xu, D. Z. Zhang, S.-H. Chang, S. T. Ho, E. W. Seelig, X. Liu, and R. P. H. Chang, Phys. Rev. Lett. 84, 5584 (2000)

[3] R. K. Thareja, and A. Mitra, Appl. Phys. B 71, 181 (2000)

[4] M. H. Huang, S. Mao, H. Feick, H. Yan, Y. Wu, H. Kind, E. Weber, R. Russo, and P. Yang, Science 292, 1897 (2001)

[5] P. Yang, H. Yan, S. Mao, R. Russo, J. Johnson, R. Saykally, N. Morris, J. Pham, R. He, and H. J. Choi, Advanced Functional Materials 12, 323 (2002)

[6] R. Yan, D. Gargas, and P. Yang, Nature Photon. 3, 569 (2009).

[7] S. Chu, G. Wang, W. Zhou, Y. Lin, L. Chernyak, J. Zhao, J. Kong, L. Li, J. Ren, and J. Liu, Nature Nanotechnology 6, 506 (2011)

[8] Z. K. Tang, G. K. L. Wong, P. Yu, M. Kawasaki, A. Ohtomo, H. Koinuma, and Y. Segawa, Appl. Phys. Lett. 72, 3270 (1998)

[9] S. Cho, J. Ma, Y. Kim, Y. Sun, K. L. Wong, and J. B. Ketterson, Appl. Phys. Lett. 75, 2761 (1999)

[10] S. Chu, M. Olmedo, Z. Yang, J. Kong, and J. Liu, Appl. Phys. Lett. 93, 181106 (2008)

[11] C. Yuen, S. F. Yu, S. P. Leong, H. Y. Yang, S. P. Law, N. S. Chen, and H. H. Hng, Appl. Phys. Lett. 86, 031112 (2005)

[12] H. Cao, Y. G. Zhao, S. T. Ho, E. W. Seelig, Q. H. Wang, and R. P. H. Chang, Phys. Rev. Lett. 82, 2278(1999)

[13] H. Yan, R. He, J. C. Johnson, M. Law, R. J. Saykally, and P. Yang, J. Am. Chem. Soc. 125, 4728 (2003)

[14] D. J. Gargas, M. E. Toimil-Molares, and P. Yang, J. Am. Chem. Soc. 131, 2125 (2009)

[15]J. Fallert, R. J. B. Dietz, H. Zhou, J. Sartor, C. Klingshirn, and H. Kalt, Phys. Status Solidi C 2, 449 (2009)

[16]L. K. Vugt, S. Ruhle, and D. Vanmaekelbergh, Nano Lett. 6, 2707 (2006)

[17]Y. Wei, W. Wu, R. Guo, D. Yuan, S. Das, Z. Wang, Nano Lett. 10, 3414 (2010)

[18] S. Zhang, Y. Shen, H. Fang, S. Xu, J. Song, and Z Wang, J. Mater. Chem. 20, 10606 (2010)

[19] A. Das, J. Heo, M. Jankowski, W. Guo, L. Zhang, H. Deng, and P. Bhattacharya, Phys. Rev. Lett. 107, 066405 (2011)

[20] J. Carroll, J. Whiteaway, and D. Plumb, Distributed feedback semiconductor lasers, Redwood Books, Trowbridge (1998)

[21] R. French, R. Abou-Rahme, D. Jones, L. McNeil, Solid State Optical Materials, 28, 63 (1992)

[22] V. Anjos, A. Andrade, M. Bell, Appl. Surface Sci. 255, 698 (2008)

[23] R. Einhaus, F. Duerinckx, E. Kerschaver, J. Szlufcik, F. Durand, P. Ribeyron, J. Duby, D. Sarti, G. Goaer, G. Le, I. Perichaud, L. Clerc, S. Martinuzzi, Mater. Sci. and Engineering: B, 58, 81 (1999)

[24] D. Klein, Characterization and improvement of silicon solar cells: Enhanced light acceptance and better separation and extraction of charge-carriers, 74 (2009)

[25] X. Gao and L. Wang J. Am. Chem. Soc. 125, 11299 (2003)

[26] J. Wu and S. Liu, Adv. Mater. 14, 215 (2002)

[27] Z. Chen, Z. Shan, M. Mao, L. Lu and S. Mao, Nanotechnology, 15, 365 (2004)

[28] D. O'Carroll, I. Lieberwirth, and G. Redmond, Nature Nanotechnology 2, 180 (2007)

A. B. Djurisic. Y. H. Leung, Small 2, 944 (2006)

[29] A. B. Djurisic. Y. H. Leung, Small 2, 944 (2006)

[30] V. V. Ursaki, V. V. Zalamai, I. M. Tiginyanu, A. Burlacu, E. V. Rusu, and C. Klingshirn, Appl. Phys. Lett. 95, 171101 (2009)

[31] S. Ruhle, L. K. van Vugt, H. Y. Li, N. A. Keizer, L. Kuipers, and D. Vanmaekelbergh, Nano Lett. 8, 119 (2008)

[32] V. S. Park, and J. R. Schneider, J. Appl. Phys. 39, 3049 (1968)

[33] L. Chen, and E. Towe, Appl. Phys. Lett. 89, 053125 (2006)

[34] J. C. Johnson, H. Yan, P. Yang, and R. J. Saykally, J. Phys. Chem. B 107, 8816 (2003)

Chapter VI Development of ZnO based laser diode

6.1 Introduction

Lowering threshold current is a key goal on which scientists and engineers put a great deal of efforts in the past half century, since the first LD based on GaAs p-n junction structure was reported.[1] A breakthrough in electrically pumped devices came from the idea of double heterojunction structure, which realizes coincidence and concentration of recombination, light emission and population inversion in the same gain layer, hence the dramatic decrease of threshold current, however, it is still too high for many applications. [2,3] For wide band-gap semiconductor materials, a high carrier concentration is usually required in order to reach an optical gain that is high enough for lasing action in an electron-hole plasma (EHP) process.[4] The EHP mechanism, which is common for conventional LD operation, typically requires high threshold current density. Exciton lasing, as an alternative, is a more efficient radiative process and can facilitate low-threshold stimulated emission owing to its bosonic nature.[5] However, in some semiconductor materials such as III-V nitride and GaAs, the exciton binding energies are too small to sustain thermal interruption, so excitonic emission was only observed in the low-dimensional structures.[6,7] In contrast, ZnO has a native exciton binding energy of 60 meV, which enables excitonic gain even without low dimensional quantum confinement.[8]

Although ZnO has potential as an alternative to III-V nitride, it is still underdeveloped due to the difficulty of p-type doping, [9] which hinders the realization of electrically pumped LDs. Compared to electrically pumped cleaved-crystal GaN diode

laser, most ZnO lasers are unconventional, including optically pumped disordered particles, [10] optically pumped nanowires, [11] and electrically pumped metal-oxide-semiconductor laser.[12] Electrically pumped pn-junction laser diodes using ZnO-based heterostructures have been rarely reported.[13,14]

In this chapter, we developed random laser from a diode with embedded MgZnO/ZnO/MgZnO double heterostructure (DH), where the MgZnO barrier is relatively thick and the ZnO well is smaller than the structure in Chapter IV. We also developed electrically pumped laser for ZnO nanowires with metal-insulator-semiconductor structure assisted by DBR.

6.2 Random laser from MgZnO/ZnO double heterostructure

6.2.1 Device structure

Figure 6.1 shows a schematic of the ZnO based DH device. The structure was grown on n-type Si (100) substrate (1-20 Ω·cm) using plasma-assisted molecular beam epitaxy (MBE). A thin magnesium oxide (MgO) buffer layer was first deposited at 350 ºC to reduce the lattice mismatch between Si and ZnO, followed by 200 nm Ga-doped n-ZnO at 550 ºC. After the growth of n-ZnO, a $Mg_{0.1}Zn_{0.9}O$/intrinsic ZnO/$Mg_{0.1}Zn_{0.9}O$ heterostructure was grown. Subsequently, the temperature was increased to 600 ºC and 200nm Sb-doped p-ZnO was grown. High-temperature post-annealing at 750 ºC was performed to activate acceptor dopants.

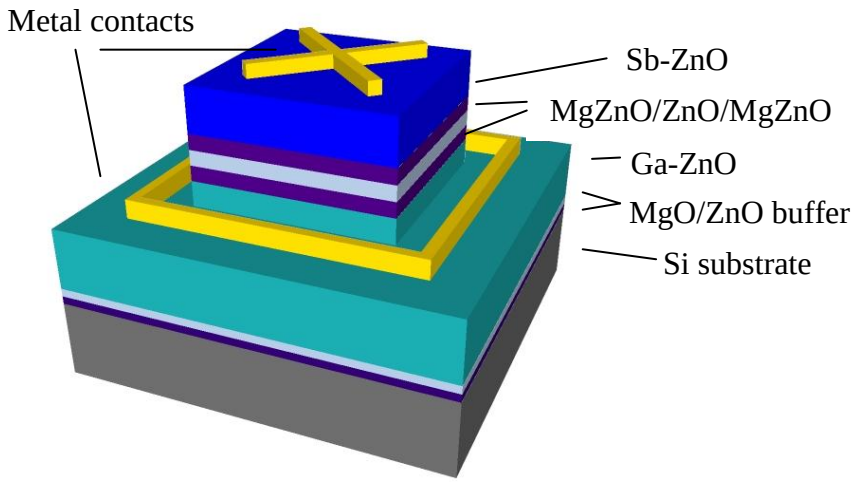

Figure 6.1 Schematic of the LD device

6.2.2 Device characterization

As-grown sample exhibits loosely packed columnar structures with in-plane size of 200 nm on average as a result of large lattice mismatch between Si and ZnO, which are clearly seen in the scanning electron microscope (SEM) image in the inset of Fig. 6.2 (a). Figure 6.2 (a) shows x-ray diffraction (XRD) θ/2θ scan spectrum of the diode, indicating that the film grows preferentially along the c-direction of the ZnO wurtzite lattice. The sample was etched down to Ga-doped ZnO layer via standard photolithography process and mesa of 800μm×800μm was defined. Au/Ti and Au/NiO were deposited on the bottom Ga-doped layer and top Sb-doped layer, respectively, after which the proper temperature annealing was carried out to form good Ohmic contacts.

The elemental distribution of Zn, O, Mg, Ga, Sb and Si was obtained by performing secondary ion mass spectroscopy (SIMS) measurements, and the result is shown in

Fig.6.2 (b). Clear MgZnO/ZnO/MgZnO structure is inferred at around 200 nm depth under surface. The ZnO well width was determined to be 30 nm. Also, Sb signal extends from the top ZnO layer into upper MgZnO layer, which may give rise to a more efficient hole supply reservoir. Due to diffusion of Mg, the SIMS profile shows broad signals.[15] Strong Mg signal near the interface of ZnO and Si substrate indicates the existence of MgO/ZnO buffer layer.

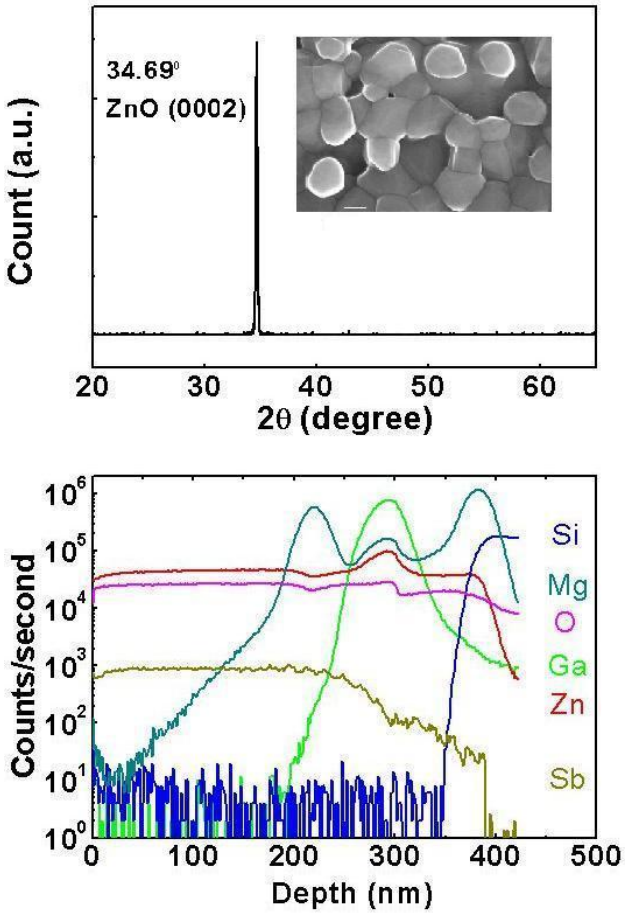

Figure 6.2 (a) XRD θ/2θ result showing preferential (0001) growth. Inset is top-view SEM image of as-grown sample. (b) SIMS spectra of the sample, showing elemental distribution of Zn, O, Mg, Ga and Sb.

Figure 6.3 shows the current-voltage characteristics of the laser device. The insets show Ohmic behaviors of n-contacts and p-contacts. The rectifying characteristic between n- and p-contacts suggests that a p-n diode should be formed. Turn-on voltage can be determined to be about 5V. Lasing emission was collected from mesa surface as the diode was biased under DC forward voltages.

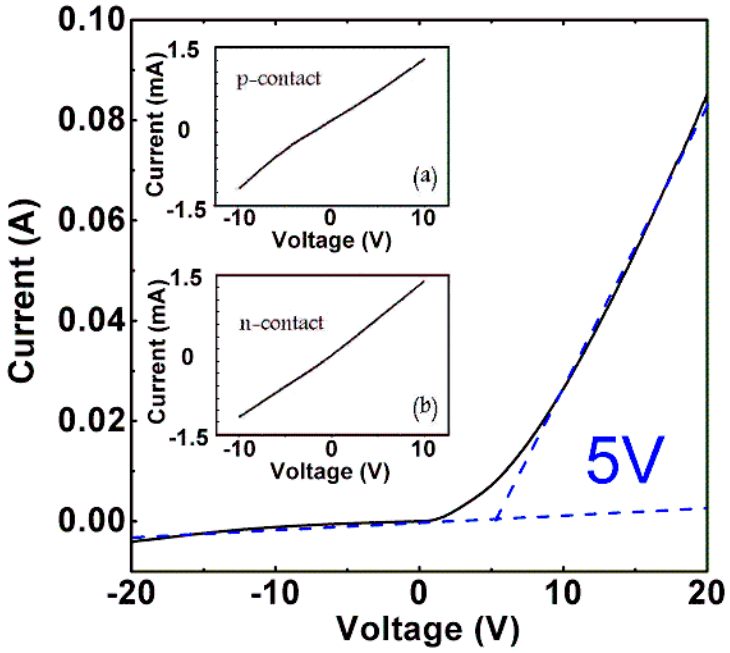

Figure 6.3 current-voltage characteristic of a typical diode. Insets show that Ohmic contacts were formed for p-type ZnO layer and n-type ZnO layer, respectively.

Figure 6.4 shows the electroluminescence (EL) spectra of the diode. Clear lasing occurs as drive current increases above 30 mA. Both the number and intensity of sharp lasing mode peaks in the spectra region increase as the injection current increases. Some lasing modes also disappear at the higher injection currents. The lasing modes are

determined by the path of the close loop random cavities. Since the close loops are randomly formed by scattering, it is possible that under different injection currents, the paths of close loops are different. Overall, there is higher possibility of the formation of additional random cavities at higher currents. It is a typical phenomenon for random laser, and is widely observed in electrically pumped and optically pumped ZnO based devices.[10-12] The top inset shows the typical full wavelength EL spectrum from the device, which covers from 350 nm to 650 nm. Near band edge emission is dominant compared to weak deep level emissions.

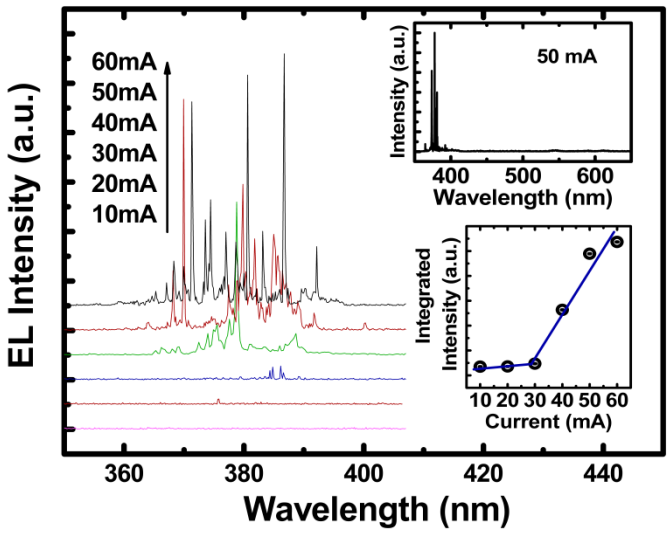

Figure 6.4 Room temperature EL spectra at the injection current from 10 mA to 60 mA. The top inset is a typical full wavelength recording, showing no deep level emission, and the bottom inset is integrated intensity vs. injection current.

6.2.3 Discussion

There is no indication of EHP formation since the center of lasing peaks is almost at the same position of 380 nm when the injection current increases from 10 mA to 60 mA, as shown in Fig.6.4. In normal EHP case, EHP recombination comes at the lower energy tail of excitonic emission, and has an evident red-shift as pumping power increases,[16,17] which is mainly due to band gap renormalization with excess carrier density larger than Mott density.

The plot of the integrated lasing spectrum intensity as a function of injection current is shown in the lower inset of Fig.6.4. A solid line is plotted to guide the eyes, showing the threshold current of about 30 mA, corresponding to current density of 4.7 A/cm^2. The threshold current density is given approximately by $J_{th}=eN_{th}d/\tau$, where e is the electron charge, N_{th} is the carrier density at the threshold, d is the active layer thickness. Assuming the exciton lifetime of 100 ps,[18] and the active layer thickness of 30 nm according to the SIMS profile, N_{th} is calculated to be 3×10^{15}cm^{-3}. This number is much less than the Mott density of 5×10^{17} cm^{-3} in ZnO,[19] suggesting that the gain in this diode laser should originate from excitonic process rather than EHP process. Low hole carrier concentrations may be enough for excitonic lasers from a theoretical prediction.[8] For Sb doping, higher hole concentration of up to 10^{18} cm^{-3} was achieved,[20] therefore, it confirms that p-type doping of ZnO, although difficult, may create sufficient hole carrier concentrations for realizing low-threshold electrically pumped random lasers. It should be noted that this estimation does not consider the current crowding effect where mesa edge and center areas carry larger current density

than other areas on the mesa due to the current spreading from bottom electrode and top electrode, respectively. Nevertheless, we argue that the current density near the mesa edge areas is still not large enough to generate EHP process as the lasing spectra does not red-shift at higher injection currents.

A dynamic view of excitonic recombination is plotted in Fig. 6.5(a). At the forward bias condition, electrons and holes are injected from Ga-doped ZnO layer and Sb-doped ZnO layer, respectively, and trapped into the central ZnO well layer within MgZnO barriers. Recombination occurs mainly in the central ZnO layer, where electrons and holes form excitons through the electron-hole Coulomb interaction. Further injection of electrons and holes into the ZnO well at higher biases leads to carrier-exciton interaction with photon emissions and gain.

In addition to the formation of optical gain, light multiple scattering to form close loops to amplify stimulated emission is required in random lasing. In this device, as schematically shown in Fig. 6.5 (b), the close loops could be formed by random scattering via vertical column boundaries in the thin film, with pores or air gaps in between each other, acting as multi-faceted scattering media; or back-and-forth reflections at the parallel side walls. These air gaps play important roles in enhancing the light scattering due to its refractive index difference with ZnO; without these air gaps, the diodes with similar MgZnO/ZnO/MgZnO heterostructures showed no lasing or weak lasing on Si and sapphire substrates, respectively.[21,22] Since the column boundary planes are vertical to the substrate, the light close-loops are formed in the film plane

rather than in the growth direction, leading to edge emission, rather than surface emission. [23,24]

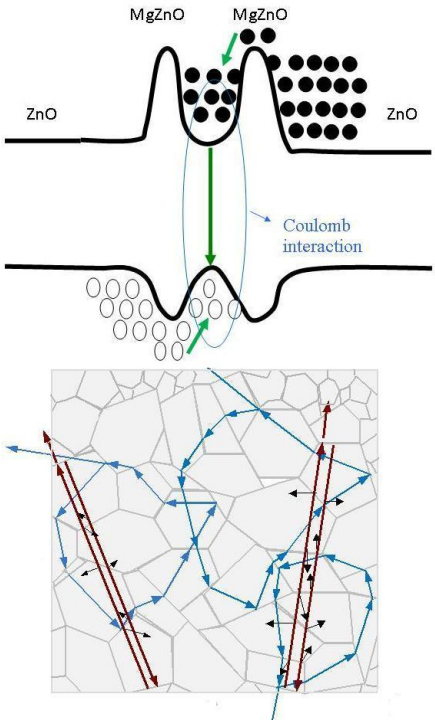

Figure 6.5 (a) Band diagram and dynamic view of exciton formation and electron-exciton interaction process. (b) Schematic view of random laser close loops from light multiple scattering, including random scattering from multiple planes and two parallel planes.

An image of a working device at drive current of 30 mA was taken by microscope camera in dark background, as shown in Fig. 6.6(a). The edge emission is dominant compared to surface emission, indicating that the close loops are indeed formed in the film plane. Note that a conventional edge emitting LD normally requires the polishing of the edge or perfect cleave of the crystal, [25] however, in ZnO case, the perfect cleavage along parallel crystal planes is difficult as its hexagonal crystal structures would not be as easily cleaved with flat planes as those cubic crystals. In the present LD, no polishing

process was done on the edge except a standard mesa wet chemical etching in the device fabrication process. Therefore, side planes of the diode mesa are not completely perpendicular to the substrates, as shown in the SEM image in Fig. 6.6(b). Figure 6.6 (c) draws possible paths for a scattered light from a close loop to escape from the device. It is evident that once the lasing light, a refracted light from an in-plane close-loop random cavity, is incident to the titled and rough edge plane of the mesa, it will be reflected/refracted by this plane to emit onto all directions.

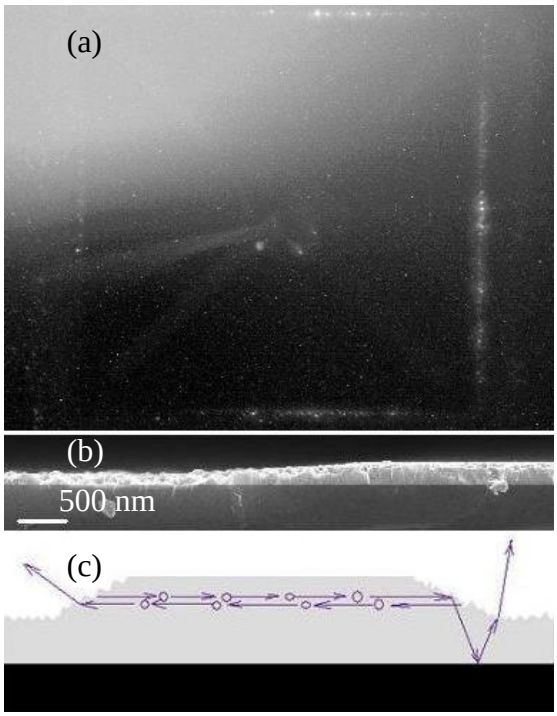

Figure 6.6 (a) Image of a working device taken by microscope camera at dark background with drive current 30 mA. (b) SEM side view of mesa edge of the diode. The dashed line, which is on the same plane of the mesa surface, is drawn to guide the eyes to see the tilted and rough mesa edge plane. (c) Schematic explanation of the output paths of scatgtered lights. Only one close-loop is drawn for clarity.

6.2.4 Conclusion

We experimentally realized an electrically pumped random laser with a MgZnO/ZnO/MgZnO heterostructure embedded in a ZnO p-n junction at room temperature. Due to excitonic process, threshold current is low. Moreover, naturally grown columns provide multiple scattering media at boundaries, giving rise to the formation of random close loops, hence the laser has randomly distributed peaks. The observation of random laser in this device confirms the recent achievement of p-type doping is sufficient for realization of low-threshold electrically pumped laser.

6.3 DBR assisted ZnO nanowire laser diode with metal insulator semiconductor structure

6.3.1 Introduction

Optical pumping experiments in the previous chapter have proved that introducing DBR structure lowers pumping threshold power. The next step is to realize low threshold electrically pumped Fabry-Perot laser. The best solution would be to grow p-type ZnO nanowires on n-type ZnO butter layer, as we reported before. [26] However, p-type ZnO nanowires are difficult to achieve on DBR structure. The main reason is that the buffer layer grown on SiO2 has low quality compared to the buffer layer grown on sapphire substrate, leading to the difficulty of acceptor doping. To avoid the problem, the metal insulator semiconductor structure is proposed here. The insulator layer worked as the confinement barrier to local high concentration of electrons, which recombine with the holes coming from the other side. The cavity of random laser is distributed in any directions in between the top metal and the bottom DBR. The outgoing laser emission is

only observed at the edge of the metal. For Fabry-Perot type laser, since the cavity is vertically formed, the exit lasing emission will be along the nanowire c axis. Here arises another problem, that the metal deposited on top of nanowires will block the lasing emission outgoing. To solve this problem, we use NiO instead of gold as the metal for hole injection. Thin layer of NiO has abundant holes naturally and is transparent in UV. [27,28]

6.3.2 Device fabrication

The vertically aligned ZnO nanowires with different lengths were grown by CVD method. To form the barrier layer for the subsequent MIS device, the nanowires was then transferred on the atomic layer deposition (ALD) furnace for Al_2O_3 deposition. The sources were water, and aluminum tetrachloride ($AlCl_4$). The growth temperature was 150°C under low pressure with a 15 sec waiting time between the sources. The Al_2O_3 was deposited both at the top ends and on the sidewalls of the nanowires, so the entire nanowire was coated by 10 nm Al_2O_3. PMMA was used to fill the gaps of the nanowires and 20 nm NiO was then deposited on the coated nanowires to form top contact by E-beam evaporation. Ti/Au was deposited on ZnO buffer layer where there is no nanowires grown on, and proper annealing was performed to form Ohmic contact. Figure 6.7 shows the device fabrication steps.

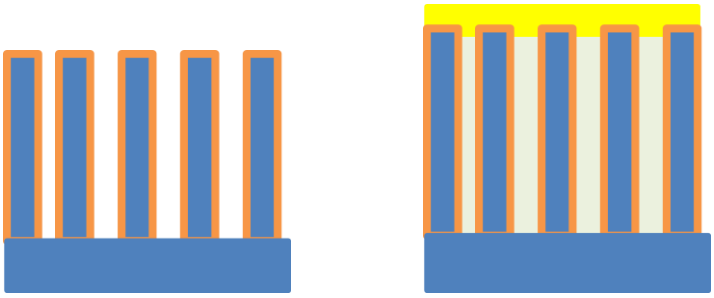

Figure 6.7 Schematic of fabrication of metal oxide semiconductor diode

6.3.3 Device characterization

The device works when the positive bias is applied at the top Au electrode. The negative bias is applied on ZnO buffer layer 2 mm away the disordered nanowires, and the positive bias is applied on top of ZnO nanowires through Indium Tin oxide (ITO) glass. The current goes through ZnO polycrystalline layer since the vertically aligned nanowires are disconnected with each other.

Figure 6.8 shows the electroluminescence (EL) spectra of one device with an average cavity length of 10 um at the injection current from 15 mA to 30 mA. When the injection current goes up to 15 mA, a broad peak emission with a center wavelength of 385 nm starts to show up, originating from ZnO band edge recombination. As the injection current goes up to 20 mA, the intensity of this broad peak emission becomes stronger and several sharp peaks with full width at half maximum (FWHM) of about 0.5 nm arise upon the broad peak, indicating the on-set of stimulated random laser emission. When the injection current goes higher, the lasing peaks are stronger and sharper. The center of multiple lasing peaks redshifts as injection current goes up from 15 mA to 30 mA. Unlike optical pumping, not every mode shows up during each measurement. Noted that most of the lasing peaks have stable positions with slight blue shift due to heat

induced refractive index variation [29], indicating the formation Fabry-Perot resonant cavity instead of random cavity. The mode space of this sample is about 1.4 nm, which is very close to the calculated mode space (1.2 nm).

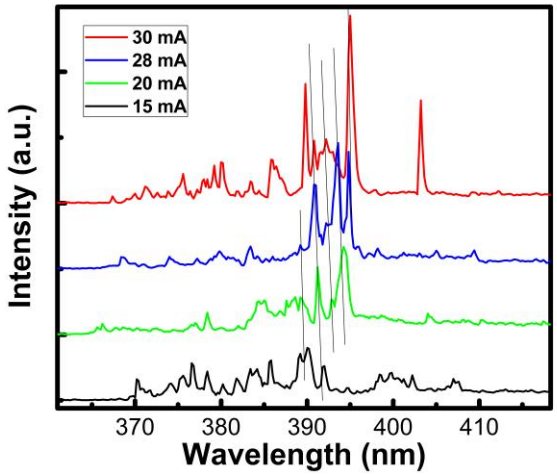

Figure 6.8 Electroluminescence from 10 um nanowire MIS structure diode at different injection current

Another nanowire device which has an average cavity length of 4 um was performed the same EL experiment. The major lasing peaks were aligned by solid lines, showing the mode space of about 2.5 nm, as shown in Fig. 6.9. Although the two different lengths nanowire devices show Fabry- Perot characteristic, they are not standard Fabry- Perot type laser. The lasing modes are not stable at different injection current. Although the Fabry-Perot cavity may work as the resonant cavity, the emission is from multiple cavities. It is possible that only a few cavities lase from each experiment, thus some randomly magnified modes are observed. In this case, although Fabry-Perot cavity

participated in lasing, it still can be classified to random laser because the detected modes are randomly selected.

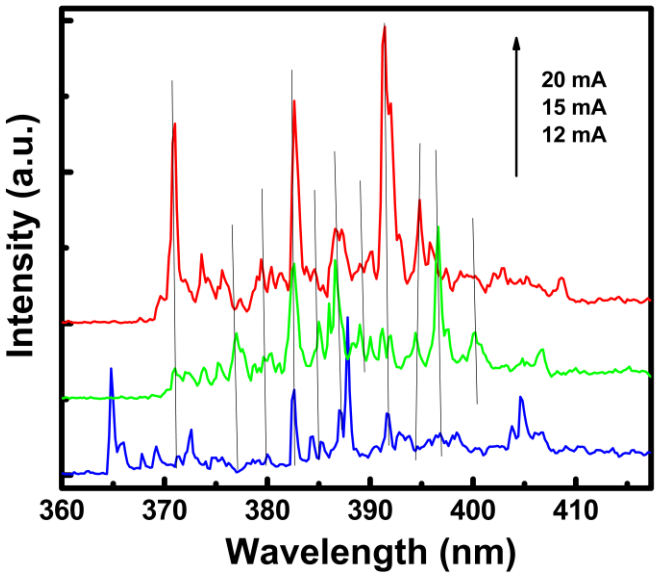

Figure 6.9 Electroluminescence from 4.5 um nanowire MIS structure diode at different injection currents

Figure 6.10 shows a schematic view of lasing mechanism. The band gap of Al_2O_3 is 7 to 10 eV,[30] which acts as a barrier in the band structure. Under positive bias, the holes in the Au gate electrode tunnel through the Al_2O_3 barrier into ZnO.[31,32] Meanwhile, the electrons from the semiconductor drift in the opposite direction. The existing high barrier of Al_2O_3 accumulates electrons in the insulator-semiconductor interface well, which acts as the recombination region. Although the tunneling holes drift towards inner part of semiconductor by the electric field, they are blocked by the Al_2O_3 layer at the other side. Moreover, the effective mass of the holes is relatively large.[33] Considering the picosecond lifetime of the excited electron-hole pairs,[34] a large amount

of electrons and holes will recombine near the semiconductor surface to either emit light or heat.

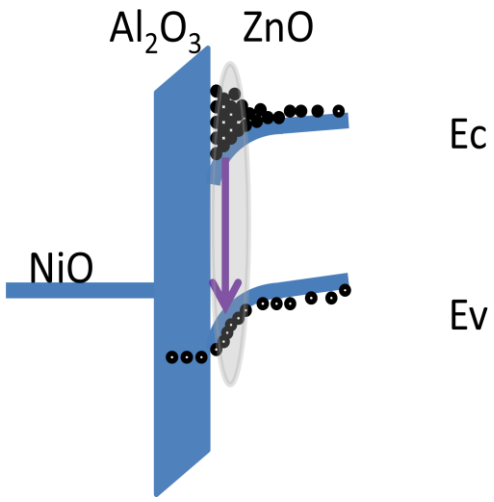

Figure 6.10 Diagram at positive bias and dynamic view of the recombination.

6.3.4 Conclusion

DBR assisted ZnO nanowire laser diode with metal insulator semiconductor structure was achieved. By using NiO as the hole supplier and utilizing insulator barrier to confine the electrons, lasing emissions were observed on the surface of the nanowires. The lasing mode space is strongly related to the cavity length, and roughly follows the inverse relation according to the results from two different devices with cavity length of 10 um and 4 um respectively. Although the lasing modes indicate Fabry-Perot type resonant cavity, they are not stable at different injection currents. The randomly selected output modes classify it to be random lasing.

6.4 references

[1] R. N. Hall, G. E. Fenner, J. D. Kingsley, T. J. Soltys, and R. O. Carlson, Phys. Rev. Lett. 9,366 (1962).

[2] Zh. I. Alferov and R. F. Kazarinov, Inventor's Certificate No. 181737 (in Russian)

[3] H. Kroemer, Proc. IEEE 51, 1782 (1963).

[4] C. Klingshirn, J. Cryst. Growth 117, 753 (1992).

[5] A. Imamoglu, R. J. Ram, S. Pau and Y. Yamamoto, Physical Rev. A, 53, 4250 (1996).

[6] W. Wegscheider, L. N. Pfeiffer, M. M. Dignam, A. Pinczuk, K. W. West, S. L. McCall, and R. Hull, Phys. Rev. Lett, 71, 4071 (1993).

[7] S. F. Chichibu, T. Azuhata, T. Sota and T Mukai, Appl. Phys. Lett. 79, 341 (2001).

[8] M. Zamfirescu, A. Kavokin, B. Gil, G. Malpuech, and M. Kaliteevski, Phys. Rev. B 65, 161205(R) (2002).

[9] C. G. Van de Walle, Phys. Rev. Lett. 85, 1012 (2000).

[10] H. Cao, Y. G. Zhao, H. C. Ong, S. T. Ho, J. Y. Dai, J. Y. Wu, and R. P. H. Chang, Appl. Phys. Lett. 73, 3656 (1998).

[11] M. H. Huang, S. Mao, H. Feick, H. Yan, Y. Wu, H. Kind, E. Weber, R. Russo, P. Yang, Science, 292, 1897 (2001).

[12] X. Ma, P. Chen, D. Li, Y. Zhang and D Yang, Appl. Phys. Lett. 91, 251109 (2007).

[13] S. Chu, M. Olmedo, Z. Yang, J. Kong and J. Liu, Appl. Phy. Lett. 93, 181106 (2008).

[14] Y. R. Ryu, J. A. Lubguban, T. S. Lee, H. W. White, T. S. Jeong, C. J. Youn, and B. J. Kim, Appl. Phys. Lett. 90, 131115 (2007).

[15] Claus Klingshirn, Johannes Fallert, Huijuan Zhou, and Heinz Kalt, Appl. Phys. Lett. 91, 126101 (2007).

[16] J. Dai, C. X. Xu, P. Wu, J. Y. Guo, Z. H. Li and Z. L. Shi, Appl. Phys. Lett. 97, 011101 (2010).

[17] M. Kawasaki, A. Ohtomo, I. Ohkubo, H. Koinuma, Z. K. Tang, P. Yu, G. K. L Wang, B. P. Zhang, Y. Segawa, Materials Science and Engineering B56, 239 (1998)

[18] T. Koida, S. F. Chichibu, A. Uedono, A. Tsukazaki , M. Kawasaki, T. Sota, Y. Segawa and H.Koinuma, Appl. Phys. Lett. 82, 532 (2003)

[19] C. Klinshirn, R. Hauschild, J. Fallert and H. Kalt, Phy. Rev. B 75, 115203 (2007)

[20] F. X. Xiu, Z. Yang, L. J. Mandalapu, D. T. Zhao, J. L. Liu and W. P. Beyermann, Appl. Phys. Lett. 87, 152101 (2005)

[21] S. Chu, J. Zhao, Z. Zuo, J. Kong, L. Li and J. Liu, J. Appl. Phys. 109, 123110 (2011)

[22] J. Kong, L. Li, Z. Yang, J. Liu, J. Vac. Sci. Technol. B 28(3), C3D10, (2010)

[23] S. Gottardo, S. Cavalieri, O. Yaroshcuk, D. S. Wiersma, Phys. Rev. Lett. 93, 263901 (2004).

[24] S. P. Lau, H. Y. Yang, S. F. Yu, H. D. Li, M. Tanemura, T. Okita, H. Hatano, Appl. Phys. Lett. 87, 013104 (2005).

[25] S. Nakamura, M. Senoh, S. Nagahama, N. Iwasa, T. Yamada, T. Matsushia, H. Kiyoku, Y. Sugimoto, T. Kozaki, H. Umemoto, M. Sano, K. Chocho, Appl. Phys. Lett. 73, 832 (1998).

[26] S. Chu, G. Wang, W. Zhou, Y. Lin, L. Chernyak, J. Zhao, J. Kong, L. Li. J. Ren and J. Liu, Nature Nanotechnology, 6, 506 (2011).

[27] R. J. Powell and W. E. Spicer, Phys. Rev. B 2, 2182 (1970)

[28] P. W. Tasker and D. M. Duffy, Surface Science, 137, 91 (1984)

[29] V. S. Park, and J. R. Schneider, J. Appl. Phys. 39, 3049 (1968)

[30] R. H. Frehch, H. Mullejans, and D. J. Jones, J. AM. Ceram. Soc, 81, 2549-2557 (1998)

[31] T. Minami, M. Tanigava, M. Yamanishi, and T. Kawamura, Jpn. J. Appl. Phys, 13, 1479 (1974)

[32] O. Lagerstedt, B. Monemar, and H. Gislason, J. Appl. Phys, 49, 2953 (1978)

[33] G. Beni, and T. M. Rice, Phys. Rev. B18,768 (1978).

[34] Y. Zhang, R. E. Russo, and S. S. Mao, Appl. Phys. Lett. 87 133115 (2005)

Chapter VII Conclusion

UV ZnO light-emitting diode on Si (100) substrate has been realized. Reliable p-type ZnO is formed and microscopically the p-n homojunction consists of column nanostructures. Au/NiO and Au/Ti make good Ohmic contacts to p-type and n-type portions of the ZnO nano columns for the formation of LED devices. I-V and C-V measurements show good rectification behavior and EL experiments demonstrate dominant UV emissions, owing to better p-type quality. LED performance was characterized at both room temperature and 17 K, showing heat induced emission redshift and efficiency drop. To improve output power, UV MgZnO/ZnO/MgZnO double heterojunction light-emitting diode on Si (100) substrate has been realized. Au/Ni and Au/Ti make good Ohmic contacts to p-type and n-type ZnO layers. I-V measurement shows good rectification behavior and EL experiments demonstrate dominant UV emissions. Compared to ZnO homojunction diode, the output power of this device is 7.3 times stronger at the same injection current, which demonstrates a better confinement of electron and holes to recombine in an intrinsic ZnO layer.

To develop ZnO nanowire laser, 10-period DBR structure was designed using SiO_2 and SiN_x. Vertically aligned ZnO nanowires were achieved by CVD growth, on a ZnO polycrystalline seed layer deposited on DBR by MBE. Fabry-Perot type lasing was observed with optical pumping and a lower threshold excitation power was achieved due to the lower cavity loss with the DBR structure. The cavity finesses is improved and the FWHM of lasing mode is reduced. The competition between spontaneous and stimulated emission was further studied at higher pumping power. The non-extinct spontaneous

emission is due to fractional confinement of waveguide modes in small nanowires less than 100 nm in diameter. The DBR technology can be transferred to Si or even glass substrate, further lowers the cost. The achievement of lower threshold pumping power with DBR structure paves a way for further development of low-threshold ZnO nanowire laser diodes.

We also developed low threshold ZnO p-n junction laser diode with MgZnO/ZnO/MgZnO heterostructure embedded. Due to excitonic process, threshold current is low. Moreover, naturally grown columns provide multiple scattering media at boundaries, giving rise to the formation of random close loops, hence the laser has randomly distributed peaks. The observation of random laser in this device confirms the recent achievement of p-type doping is sufficient for realization of low-threshold electrically pumped laser. Moreover, DBR assisted ZnO nanowire laser diode with metal insulator semiconductor structure was achieved. By using NiO as the hole supplier and utilizing insulator barrier to confine the electrons, lasing emissions were observed on the surface of the nanowires. The lasing mode space is strongly related to the cavity length, and roughly follows the inverse relation according to the results from two different devices with different cavity lengths.